Examinations Towards X-Ray Fluorescence Tomography with the Spectroscopic Photon Counting Pixel Detector Dosepix

Master's Thesis in Physics

Presented by

Carolin Kupillas

April 6, 2023

Erlangen Centre for Astroparticle Physics
Friedrich-Alexander-Universität Erlangen-Nürnberg

Supervisor: PD Dr. Thilo Michel

Contents

1 Introduction

Since their discovery in 1895 by Wilhelm Röntgen, X-rays have been one of the fundamental clinical screening techniques with first reported clinical uses as early as 1896. Over the 20^{th} century, a multitude of different techniques bases on the Röntgens findings were developed, such as radiography, fluoroscopy, and mammography [1]. One of the groundbreaking advances in radiology came with the advent of computer tomography systems in the early 1970s, which for the first time allowed cross sectional images of a body by computer-aided reconstruction algorithms.[2]

In medical imaging, computed tomography (CT) scans cover a wide range of applications due to density contrasts, material specific contrasts and functional parameters and enable fast scans of only few seconds which achieve spatial resolutions smaller than 1 mm.[1] However, X-ray fluorescence imaging is a current field of research gaining attention for holding great promise for medical imaging applications providing additional molecular information.[3] It requires the injection of nanoparticles which serve as contrast agents.[3] Furthermore, the nanoparticles can be used to label bio-molecules and, hence, serve as markers for pharmacological processes and tumors, for example.[4] The signature of fluorescent materials is characterized by a monochromatic emission line which can be identified by spectroscopic detectors.[4] In recent years, spectroscopic photon counting detectors have been developed, such as Medipix and Timepix [5], EIGER [6] and PILATUS [7] as well as the spectroscopic photon counting pixel detector Dosepix [8]. Due to its small pixel size, Dosepix is a promising candidate regarding measurements with high flux.[9] In this thesis, a first approach of implementing Dosepix in imaging applications is given.

2 Motivation and Prospective

X-ray fluorescence tomography (XFT) is of current interest regarding the benefit on imaging labeled molecules.[4] Recent approaches to perform X-ray fluorescence imaging include monte-carlo-simulations, [10], and measurements with mice in vivo, [11], as well as postmortem, [12]. Larsson et al., [12], achieved great results combining the findings of an X-ray transmission CT with the fluorescence signal, as shown in Figure 2.1. The scanned mouse with ante mortem injected molybdenum nanoparticles as contrast agents

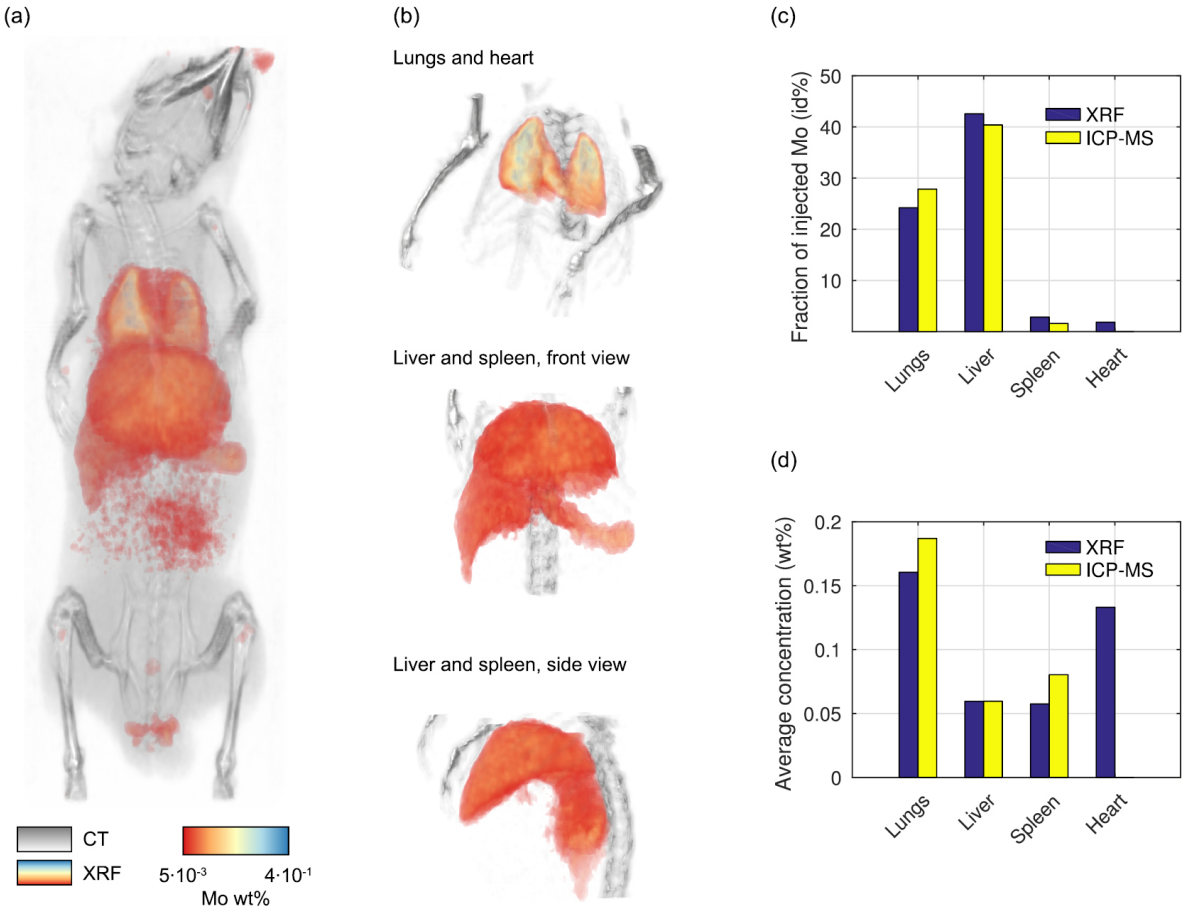

Figure 2.1: Rendered 3D view of the overlay of the XRF and CT results in (a) and some regions presented with enhanced contrast (b), quantitative molybdenum nanoparticle bio-distribution and average concentration in different organs for the mouse (c) and (d).[12]

is imaged while regions with higher concentrations of molybdenum are emphasized. The molybdenum particles accumulated to tumor regions as a result of chemical processes and, during the X-ray measurement, they serve as fluorescent medium due to the energy of the K_α emission line of molybdenum at 17.4 keV.

However, Larsson et al. describes a flux of 3×10^7 photons per second was yielded in the focus after spectrally separating the emission energy peak of the employed pencil beam X-ray source implementing a multi-layer mirror with a maximum reflectivity below 0.4 %. As a result, the CdTe absorption detector [13] had to be shielded with an aluminum filter of 11 mm thickness to surpass the maximum count rate of the detector, while the fluorescence signal in the silicon-drift fluorescence detector [14] was low.

This leads to the idea to demonstrate that the Dosepix detector is a promising solution for medical imaging applications. As introduced in the previous chapter, Dosepix is a spectroscopic photon counting pixel detector that offers high spatial resolution, excellent energy resolution, and a high count rate limit.[9]

This thesis aims to prove the fundamental capability of the Dosepix detector for computer tomography as well as x-ray fluorescence tomography applications. Therefore, a concise approach shall be presented from the introduction of the experimental setup to the collection of the X-ray and fluorescence data and, finally, the subsequent image reconstruction process. Furthermore, by combining both techniques, CT and XRF, this thesis aims to give a first outlook on the inherent potential for simultaneously determining the spatial distribution as well as concentration of molybdenum in a phantom – therefore laying the ground for future promising research in this area.

3 Theoretical Background

Contents

The theoretical background of this thesis is presented in this chapter. This includes the interactions of X-ray photons with matter as well as an overview of the X-ray creation process and the applied X-ray source.

3.1 Interactions of X-Ray with Matter

X-ray photons are called ionizing radiation, as there are interactions with matter that lead to the liberation of an electron from the binding atom.[15]

The interactions of photons with matter are crucial for this thesis. They are essential for the creation of X-ray fluorescence and are fundamental for photon detection. There are several different reactions that lead to an attenuation of X-ray photons in matter. Each photon interaction with the Dosepix sensor layer, energy is transferred from the photon to electrons which deposit their energy in the detector. In the following, the relevant interactions of photons with matter in the energy range of 10 keV to roughly 10 MeV will be explained after [16], if not stated otherwise. The referred interactions are Compton-scattering (incoherent scattering), photoelectric absorption and pair production. Furthermore, there is coherent scattering like Rayleigh- or Thomson-scattering, which is dominant for small photon energies E_{ph}, i.e. $E_{\mathrm{ph}} < E_{\mathrm{b}}$ the binding energy of an electron in

the atom. As there is no energy transferred to the atom during coherent scattering, the processes are not detectable with the Dosepix detector.

When a mono-energetic photon beam passes through matter, the intensity $I_0(E)$ of the beam gradually decreases as a result of the different interactions. This decrease $\mathrm{d}I(E,x)$ is proportional to the path length x inside a material with density ρ as described in Equation 3.1, where $\mu(E)$ is the energy-dependent mass attenuation coefficient.

$$\mathrm{d}I(E,x) = -I_0(E) \cdot \mu(E) \cdot \rho \cdot \mathrm{d}x \tag{3.1}$$

This homogeneous differential equation of first order is solved by an exponential attenuation law (Lambert-Beer law)

$$I(E,x) = I_0(E) \cdot e^{-\mu(E)\rho x}. \tag{3.2}$$

The mass attenuation coefficient of silicon as a function of incoming photon energy E_{ph} is shown in Figure 3.1. Until up to 60 keV, photoelectric absorption is the dominant interaction between photons and matter. Then, incoherent scattering is more likely until pair production becomes dominant at energies of about 10 MeV. Hence, the latter is of no relevance for this experiment, and it will be explained for completeness, only.

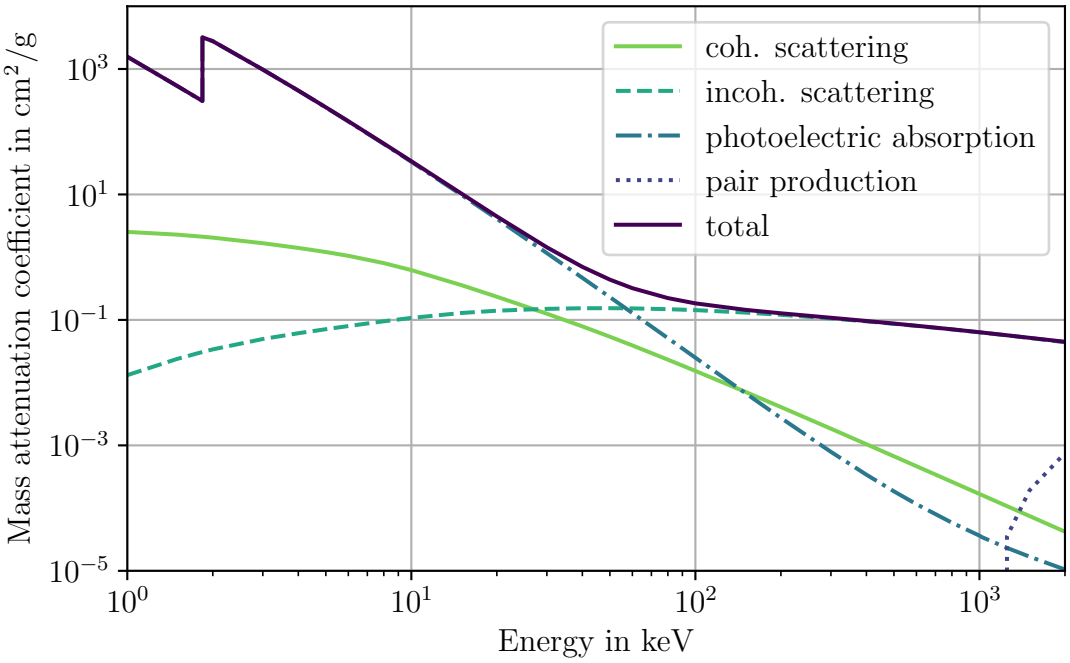

Figure 3.1: Different mass attenuation coefficients for various types of interactions with silicon as a function of photon energy. Silicon is chosen as example because it is the sensor material of the Dosepix detector that was utilized in this thesis. The data is taken from [17].

3.1.1 Photoelectric Absorption

By collision of an incoming photon of energy E_{ph} with a bound electron of the inner electron shell of an atom, the entire photon energy can be transferred to the electron. This causes the electron to leave the atom with the kinetic energy $E_{\mathrm{kin}} = E_{\mathrm{ph}} - E_{\mathrm{b}}$. Hence, the photoelectric absorption can only happen, if the energy of the photon exceeds the binding energy of the respective electron in the atom $E_{\mathrm{ph}} > E_{\mathrm{b}}$. Additionally, momentum conservation holds because momentum gets absorbed by the atom, too. Therefore, there is no photoelectric absorption for free electrons.

Equation 3.3 shows the proportionalities of the interactions cross section σ_{ph} with respect to the atomic number Z of the absorbent material and the initial photon energy for energies $E_{\mathrm{ph}} < 511\,\mathrm{keV}$ is shown. The exponent n depends on Z. For small Z, n equals 4 and for large Z, n equals 4.5.

$$\sigma_{\mathrm{ph}} \sim \frac{Z^n}{E_{\mathrm{ph}}^3} \tag{3.3}$$

The probability for photoelectric absorption is highest if the photon energy is equal or slightly greater than the corresponding binding energy of the electron. With increasing energy, the probability of the photoelectric absorption to occur decreases. As a result, the mass attenuation coefficient for materials as a function of photon energy shows absorption edges at the corresponding binding energies where the photon energy is sufficiently high to ionize electrons from stronger bound states resulting in a larger number of potential interaction partners. For silicon, the binding energy for the K-shell is 1.839 keV [18] (see in Figure 3.1). For another important element in this work, molybdenum, the binding energy of an electron in the K-shell is 20.000 keV [18].

The photoelectric effect can happen with an electron of an inner electron shell in the atom and leave the atom in an excited state. In this case, an electron of a higher energy level transitions to the state of the emitted electron and the energy difference of the levels is emitted in form of a photon. This is called characteristic radiation and explained below with more detail.

3.1.2 Compton-scattering

Compton scattering is an inelastic scattering process of a photon of energy $E_{\mathrm{ph}} = hc/\lambda$ (with h the Planck constant, c the speed of light and λ the wavelength of the photon) on a slightly bound electron in an outer electron shell of an atom. Thereby, a fraction of the photon energy and momentum is transferred to the electron. Thus, the scattered photon with wavelength λ' has smaller energy compared to the incoming photon, i.e. $\lambda' > \lambda$. The relation of the change in wavelength ($\Delta\lambda$) to the scattering angle Θ is given

by Equation 3.4, where $\lambda_c = h/(m_e c)$ is the Compton wavelength and m_e the rest mass of the electron.

$$\lambda' - \lambda = \Delta\lambda = \lambda_c(1 - \cos\Theta) \tag{3.4}$$

The energy of the scattered photon E'_{ph} is given by Equation 3.5 in dependence of the initial energy E_{ph} and the scattering angle [19]

$$E'_{ph} = \frac{E_{ph}}{1 + \frac{E_{ph}}{m_e c^2}(1 - \cos\Theta)}. \tag{3.5}$$

This means, the angular distribution of the direction of the scattered photon depends on the initial photon energy. No energy is transferred in the case of forward scattering ($\Theta = 0°$), i.e. $E'_{ph} = E_{ph}$. For back-scattering ($\Theta = 180°$), a maximum energy transfer is achieved, and the scattered photon carries the energy

$$E'_{ph} = \frac{E_{ph}}{1 + \frac{2E_{ph}}{m_e c^2}} \tag{3.6}$$

If the energy transferred exceeds the binding energy of the electron, it is ejected and leaves the atom with the kinetic energy $E_{ph} - E'_{ph} - E_b$. After Compton scattering, the scattered photon can interact again with the sensor material.

The cross section for incident photon energies E_{ph} in the range of 0.2 MeV to 10 MeV is proportional to the atomic number Z of the absorbent material and the initial photon energy to the power of n. In the case of Compton scattering, n is between 0.5 and 1.

$$\sigma_c \sim \frac{Z}{E^n_{ph}} \tag{3.7}$$

3.1.3 Pair Production

Pair production is the process of a photon decaying into an electron-positron pair in the coulomb field of an atomic nucleus. It can only happen if the photon energy is greater than twice the rest energy of an electron, $E_{ph} > 2m_e c^2 = 1.022$ MeV. The electron and positron carry the kinetic energies $E_+ = E_- = (1/2)(E_{ph} - 2m_e c^2)$. Similar to the photoelectric effect, the nucleus has to absorb momentum to ensure momentum conservation. In this thesis, only photons with lower energies than the pair production threshold are relevant. As written above, this effect is omitted in the analysis.

3.2 Working Principles of X-Ray Tubes

X-ray radiation can be produced in X-ray tubes. Here, fast accelerated electrons interact with the anode material and create X-ray radiation. In general, only 1 % of the energy of

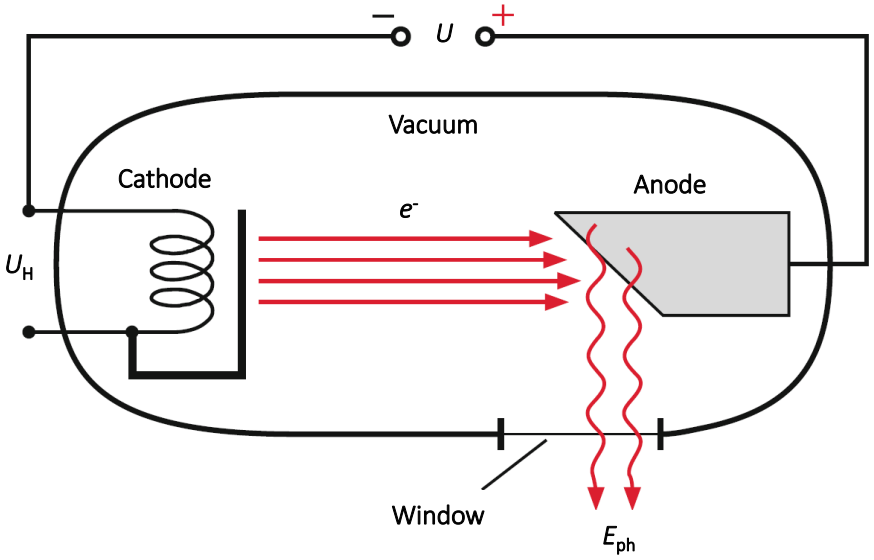

Figure 3.2: Schematic of an X-ray tube from [16]. The voltage U_{H} causes the cathode to emit the electrons that are accelerated according to the voltage U towards the anode. There, X-ray E_{ph} is created and leaves the X-ray tube through the window.

the primary electrons is transformed to X-ray radiation - the remaining 99 % of the energy are deposited in the anode material as heat.[20] A schematic of an X-ray tube is shown in Figure 3.2. The voltage U_{H} is applied to a cathode which consequently emits electrons e^-. The emitted electrons are accelerated towards the anode in the electric field between cathode and anode due to the acceleration voltage U. After passing the distance between the cathode and anode, the kinetic energy of the electrons is

$$E_{\mathrm{kin,e}} = e \cdot U. \tag{3.8}$$

Here, e is the electric charge of the electron. The X-ray tube is evacuated to reduce particle collisions The accelerated electrons interact with the anode material resulting in the emission of Bremsstrahlung radiation and characteristic radiation. Created photons leave the X-ray tube through an exit window. The physical processes leading to the two components of the emitted X-ray radiation spectrum are explained below. The emission spectrum of the utilized X-ray tube in this thesis is shown in Figure 3.4.

3.2.1 Bremsstrahlung Radiation

Bremsstrahlung is radiation with a continuous spectrum and forms the main part of the emission spectrum of an X-ray tube. Velocity changes of charged particles lead to Bremsstrahlung radiation. In X-ray tubes, Bremsstrahlung radiation is emitted when the primary electrons are decelerated in the Coulomb field of the positively charged atomic

nuclei in the anode material. The severance of deceleration increases the closer to the electron passes the atomic nucleus, so does the energy of the emitted Bremsstrahlung radiation. As high decelerations of the electrons are less likely than small decelerations, the probability for creating Bremsstrahlung radiation decreases with rising energy. This is seen in the decline of the X-ray spectrum of an X-ray tube towards higher energies. The upper energy limit of the Bremsstrahlung spectrum is determined by the maximum of transferred energy from accelerated electrons to emitted photons:

$$E_{\mathrm{ph,max}} = E_{\mathrm{e}} = e \cdot U. \tag{3.9}$$

The created X-ray radiation is attenuated by the anode material according to its creation depth. This leads to a smudged lower energy end of the created X-ray spectrum. According to [21], the penetration depth of electrons of 50 keV is (1.28±0.02) µm in tungsten anodes.

3.2.2 Characteristic Radiation

Characteristic X-ray is emitted by an atom when an electron of a higher atomic energy level E_2 transitions to a gap in the lower energy level E_1. The gap in the lower energy level is produced by different interactions. In X-ray creation, an electron or secondary Bremsstrahlung photon interacts with an electron in the atom and causes it to leave the atom. The energy difference of the two levels is emitted as photon. Hence, the emitted photon carries the energy $E_{\mathrm{x}} = E_2 - E_1$. The material specific emission spectrum of an element contains the characteristic energy peaks at the respective discrete energies of the emitted X-rays. As a result, this spectrum is called line spectrum.

For example, after an electron of the 1s orbital (K-shell) is knocked out, there is an empty position on the K-shell. This gap is filled by an electron transitioning for example from the higher energy level 2p orbital (L-shell) to the 1s orbital. Photons emitted in this special case are called K_α radiation and represent one peak in the line spectrum of the respective material.

3.2.3 Liquid Metal Jet C2 by Excillum

The X-ray tube "Liquid-Metal-Jet C2" (in the following called LMJ), sold by Excillum[22], is used as X-ray source in the experiments to this thesis. Details on the X-ray tube are taken from [23] and [22]. A sketch of the experimental arrangement of the LMJ is shown in Figure 3.3. The anode implemented in the LMJ consists of regenerative liquid indium-gallium alloy that flows with about 80 m/s. The characteristic emission peaks of gallium and indium are at 9.25 keV (Ga, K_α), 24.2 keV (In, K_α).[18] As mentioned above, the creation of X-ray in an X-ray tube involves the deposition of heat inside the anode

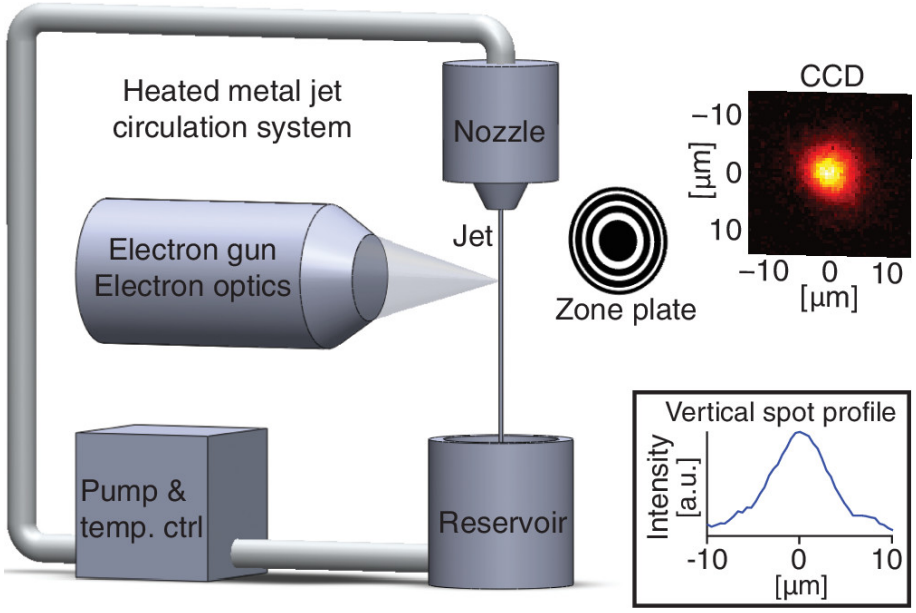

Figure 3.3: Schematic illustration of the heated metal jet circulation system in an X-ray tube of type Liquid-Metal-Jet C2 by Excillum taken from [24]. The Electron gun is the cathode of the system and emits electrons. They are accelerated towards the anode denoted with Jet. The Jet is formed in the Nozzle and flows down into the Reservoir. The pump and temperature control guarantees a steady flow by applying 180 bars of backing pressure to the Nozzle. Also, the zone plate imaging arrangement, the X-ray spot distribution measured by a charge-coupled device (CCD) camera and vertical spot profile (inset) are shown.

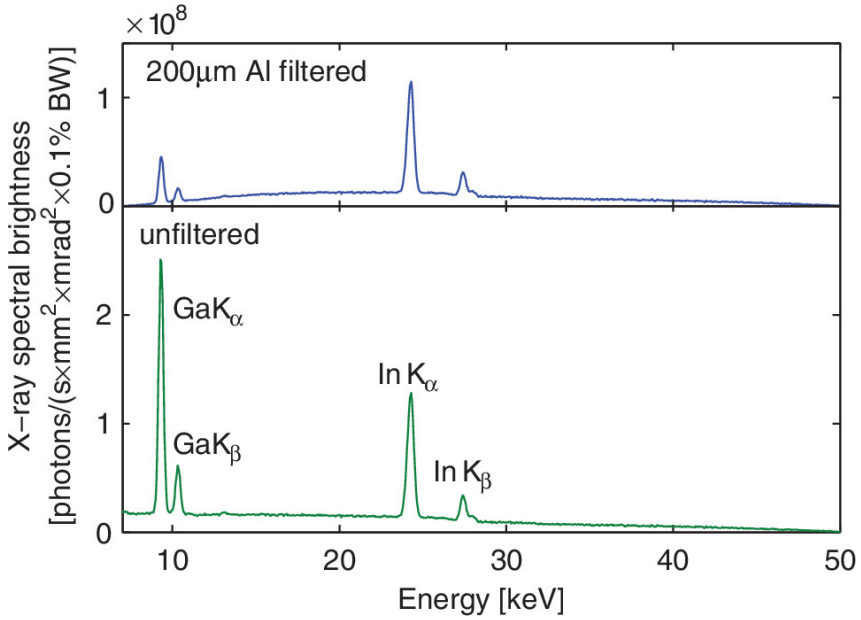

Figure 3.4: Calibrated emission spectrum recorded at 30 W with a (7×7) µm² X-ray spot. Lower curve: unfiltered spectrum. Upper curve: filtered with 200 µm Al.[24]

.

material. Therefore, the melting temperature must not be reached to avoid damaging when conventional solid anodes are used. However, the anode of the LMJ is liquid already. Hence, the deposited heat is less a problem. Also, the irradiated part of the anode (focal spot) is constantly renewed by the flow of the liquid metal jet. According to Excillum, the beam broadening of the created X-ray beam is 10.5° (beam angle).

4 Materials and Methods

Contents

This chapter gives an comprehensive overview over the materials used and methods employed in this thesis. This includes an in-depth look at the introduction of the novel hybrid spectroscopic pixel detector Dosepix. In addition, an overview of image reconstruction in the context of computed tomography is presented. Finally, the utilized phantom is introduced.

4.1 Dosepix

The hybrid photon-counting energy-resolving pixelated dead-time-free X-ray detector Dosepix is utilized in this thesis. It was developed by collaboration of FAU and CERN. All details regarding the properties of Dosepix are taken from [8], if not stated otherwise. Photographs of the Dosepix detector are shown in Figure 4.1. In part a) of the figure, a zoomed-in view of the detector is shown. In part b) the 1 ct coin serves as a reverence for the size of the detector. Dosepix is of hybrid design, thus the ASIC (application-specific integrated circuit) and segmented semiconductor sensor layer are fabricated separately and combined afterwards. A sketch of the architecture is shown in Figure 4.2. The sensor layer is doped to equally divide it into 16×16 square-shaped pixels with a pitch of 220 µm. A charge signal is created in the sensor pixels when photons interact with it. The ASIC consists also of a matrix of 16×16 pixels with a pixel pitch of 220 µm. The ASIC pixels contain charge processing frontends such that each sensor pixel has its own readout electronics. The Dosepix ASIC and the sensor layer are connected pixel-wise, mechanically and electrically, via bump bonds. Additionally, the ASIC consists of read-out

control circuits and programming blocks in the chip's periphery. The wire bonds are used to make contact between the ASIC and PCB (printed circuit board).

In this thesis, the utilized 300 µm thick silicon sensor layer with a total sensitive area of about 9.49 mm^2 consists of 16×16 p-in-n doped square pixels. In Figure 4.3, a schematic of the top view on the pixel matrix of the sensor is shown. The orientation indicated by the marked readout area matches the orientation applied in the measurements. The first two as well as the last two columns in the pixel matrix are small pixels with pixel pitch of 55 µm while the large pixels in the 12 middle columns have an edge length of 220 µm.[9] Smaller pixels are able to process higher photon fluxes due to lower expected event rate whereas large pixels provide higher statistics and better energy resolution.[26] However, in this thesis, only the large pixels are considered.

4.1.1 From Photon Interaction to Measured Energy

This subsection focuses on the interactions of primary particles with the sensor material as well as signal procession of the analogue pixel electronics.

Photon Interaction with the Sensor Material

When a photon interacts with the p-in-n silicon sensor material, the energy is transferred to a primary electron. The main effects underlying the energy deposition are Compton scattering and photoelectric absorption. As introduced in section 3.1, energy transfer to the primary electron during photoelectric absorption is the amount of energy of the incident photon minus the binding energy of the electron. Whereas, when the Compton effect happens, only a fraction of the initial photon energy is deposited to the sensor material during Compton scattering.

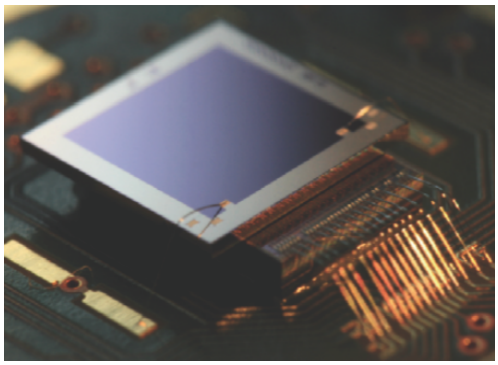

(a) Photo of the 300 µm thick silicon sensor layer on top of the ASIC and the wire bonds connecting the detector to the board on right side of the image.

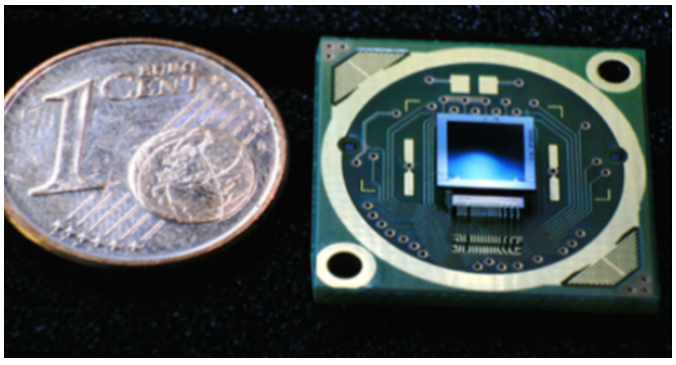

(b) A 1 cent coin next to the board containing the ASIC bump-bonded to a photon-sensitive silicon layer.

Figure 4.1: Photographs of the hybrid pixel detector Dosepix.[25]

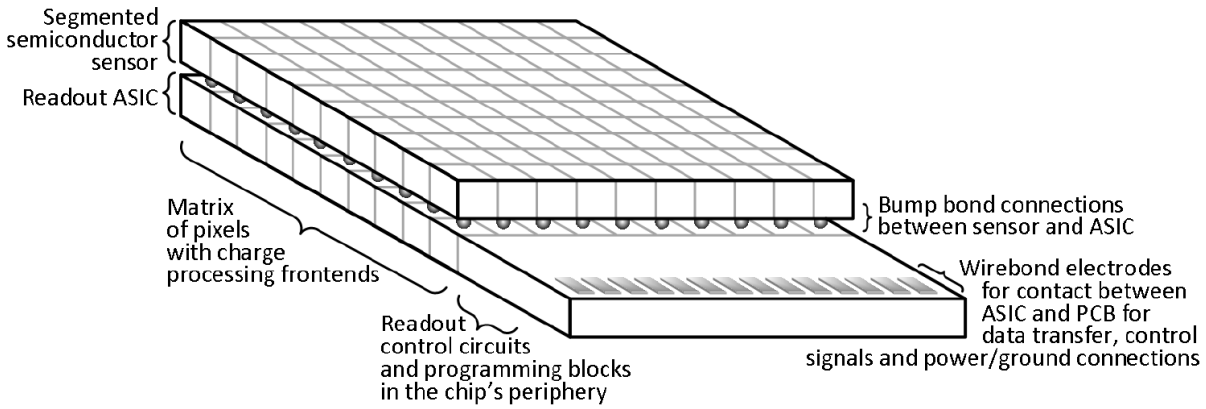

Figure 4.2: Schematic of the Dosepix detector architecture taken from [8]. The segmented silicon sensor is connected pixel-wise to the readout ASIC via bump bonds. The ASIC pixels contain charge processing frontends. Additionally, in the ASIC, there are readout control circuits and programming blocks in the chip's periphery. The wire bond electrodes connect the ASIC to the printed circuit board it is mounted upon.

The energy deposited to the semiconducting sensor material creates electron-hole pairs, where the energy for the creation is 3.62 eV [28] for silicon. In order to measure the amount of charge induced to the sensor pixel, a bias voltage is applied to the sensor pixel between the upper side of the sensor and the ASIC's side such that the holes drift to the ASIC sided end of the respective pixel.

Conversion of Charge Signal to ToT Value by the Pixel Electronics

Incoming charge signals, arriving at the pixel electronics, are converted into voltage signals by a preamplifier via integration. The output voltage is proportional to the incoming

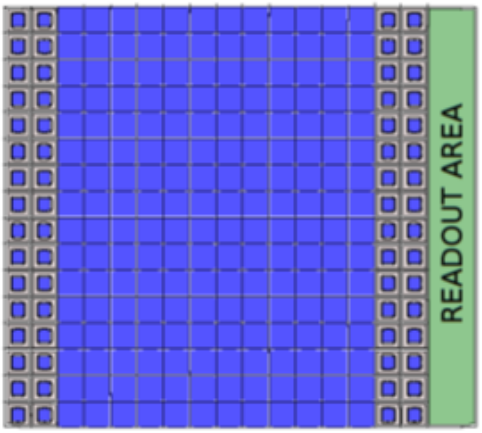

Figure 4.3: Sketch of the Dosepix sensor pixel matrix taken from [27]. The orientation of rows and columns is according to the measurements underlying this thesis.

charge. This is the signal denoted with "shaped voltage pulse" in Figure 4.5.

Hence, the voltage pulse decreases linearly with time according to the constant current I_{krum} while the slope of the decline depends on the magnitude of I_{krum}. A discriminator compares the shaped voltage pulse to an analogue threshold and sets the digital output from low to high whenever the voltage pulse exceeds the threshold. The time that it takes for the voltage signal to fall below the threshold again is measured in cycles of a 100 MHz reference clock (resolution 10 ns). The result is called the time over threshold (ToT) value and the Dosepix measure for deposited energy. In every pixel, the latest measured ToT-value is written to a register whereupon overwriting the previous one.

When charge sharing or pile-up occurs during a measurement, the ToT value does not accurately reflect the deposited energy of a single event. Charge sharing can occur when the deposited energy of an incoming photon is distributed over more than one pixel, resulting in multiple events being registered with less energy. This is illustrated in Figure 4.4. Pile-up occurs when photons interact with the pixel sensor material while

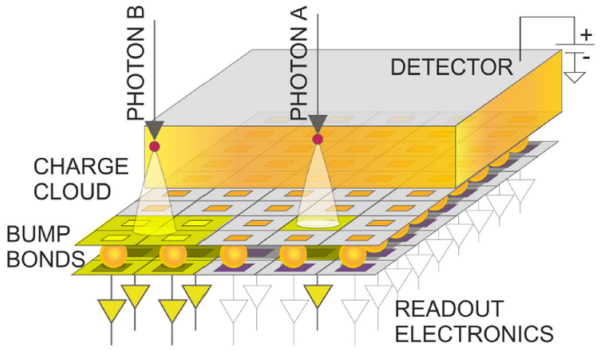

Figure 4.4: Schematic depiction of a charge sharing event (photon B) in comparison to an ideal incident (photon A).[29]

the ToT value is above threshold, resulting in an extended ToT and a measured energy that is higher than the actual deposited energy. Therefore, the energy resolution of the measurement degrades when these phenomena are present. In order to fully back-relate the ToT-value to deposited energy, a calibration needs to be carried out (see chapter 5). However, the maximum storable ToT value of 4096 counts (corresponding to 2^{12}) sets an upper limit for the registered deposited energy.

4.1.2 Data Acquisition Modes

There are three data acquisition modes that are relevant in this thesis: ToT-mode, Dosi-mode and Spec-mode. They are explained in detail in [8] and [9]. In all modes, the measurement duration is determined by the product of frame time and the number of frames.

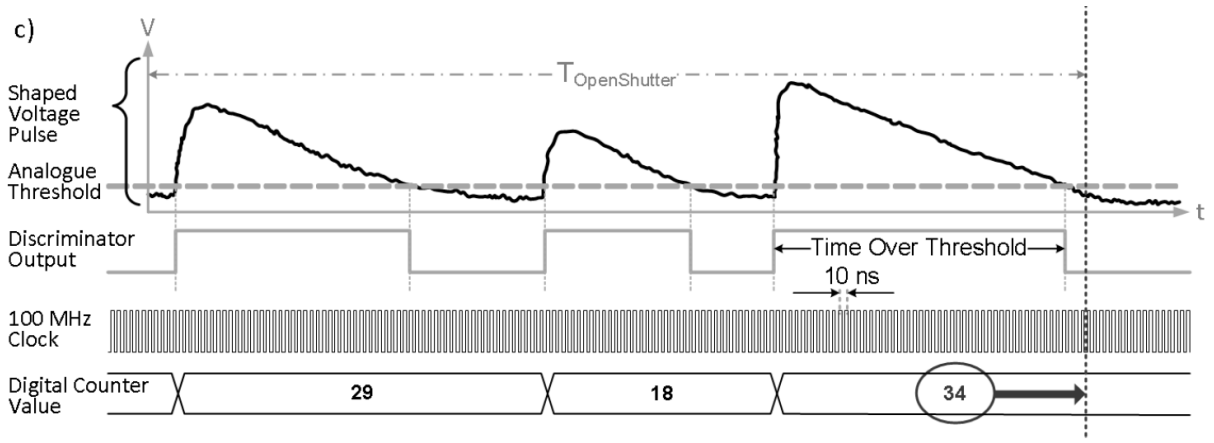

Figure 4.5: Sketch of the data acquisition process inside the Dosepix pixel electronics. When there is an event happening creating a charge signal, the preamplifier outputs the shaped voltage pulse. Once the signal is above the analogue threshold, the discriminator output changes from low to high and the discharging of the shaped voltage pulse starts as the constant current I_{krum} is applied. Once the voltage pulse falls below the analogue threshold, the discriminator output switches back to low. The duration of the high discriminator output is measured in units of clock cycles of a 100 MHz ref clock. This value is called the time over threshold (ToT) value.[8]

ToT-Mode

In this mode, the ToT-value of the latest detected event of each pixel is read after each frame. Hence, on the one hand, the acquired data has the best achievable energy resolution with the Dosepix detector regarding the determined deposited energy, on the other hand, not every detected event is saved if the event rate per pixel is higher than the read-out rate per pixel. Therefore, the received data only contains information about the shape of the energy deposition spectrum, but not about particle flux. In this thesis, the ToT-mode is solely utilized for the energy calibration of the detector.

Dosi-Mode

When an event is registered in the Dosepix detector during a Dosi-mode measurement, the deposited energy is determined via the ToT value and sorted directly into one of 16 energy bins per pixel. The last energy bin serves as an overflow bin with no upper energy limit. The remaining 15 energy bins have a user-defined lower energy limit, E_{min}, and upper energy limit, E_{max}. Solely the number of entries in each energy bin is saved pixel-wisely during each frame. Dosi-mode is "dead-time free" because it reads out individual pixel columns one after another via a rolling shutter while the other columns stay active.

The resulting output file of the python code that implements Dosi-mode contains the counted events for each energy bin, pixel and frame.

Spec-Mode

The Spec-mode is a variant of Dosi-mode described in [9]. Individual different sets of energy bins are assigned to each large pixel. The small pixels are not used in this mode. In post processing, the corresponding output file is merged to one histogram per frame over all pixels, discarding the spatial resolution of the pixel matrix of the Dosepix sensor. The advantage of this mode is narrower energy binning over the wide energy range compared to the unmodified Dosi-mode.

4.2 Image Reconstruction with Filtered Backprojection

In this section, an overview of filtered backprojection, an image reconstruction method, in the context of computed tomography (CT) is presented. Filtered backprojection denotes an analytic method for reconstructing a two-dimensional image from one-dimensional X-ray images. While conventional computed tomography systems produce two-dimensional slices of the exposed object, a three-dimensional image is only attained by stacking consecutive slices. If not stated otherwise, all details on CT imaging and reconstruction are taken from [2].

To understand the need for elaborate analysis tools like filtered backprojection, a basic image reconstruction problem for CT imaging is given in Figure 4.6. In part a) one-dimensional X-ray images are taken at two different angles γ_1 and γ_2. The detector arrays measure the produced X-ray attenuation profiles $p_{\gamma_i}(\xi)$, $i = 1, 2$ while dashed lines indicate the geometric shadow boundaries of the three exposed objects with homogeneous intersections. As for $p_{\gamma_1}(\xi)$, the X-ray attenuation profile has no gap. Therefore, it is not possible to conclude the number of objects correctly. Part b) shows a figurative illustration of the backprojection problem to find the initial radiodensity map of the scanned object. As introduced in section 3.1, when passing through a medium, the intensity of a photon beam is reduced according to Lambert-Beer's law (Equation 3.2). Modifying the Lambert-Beer law yields Equation 4.1 which describes the measured X-ray attenuation profile for a specific energy E, with the original intensity of the beam $I_0(E)$, transmitted intensity I, the material- and energy specific linear attenuation coefficient $\mu(x)$, the density of the attenuating material $\rho(x)$, and the irradiated path s between X-ray source and detector.

$$I(E, s) = I_0(E) \cdot e^{-\int_0^s \mu(E,x)\rho(x)\mathrm{d}x} \tag{4.1}$$

Taking this into account, re-arranging the modified Lambert-Beer law Equation 4.1 gives

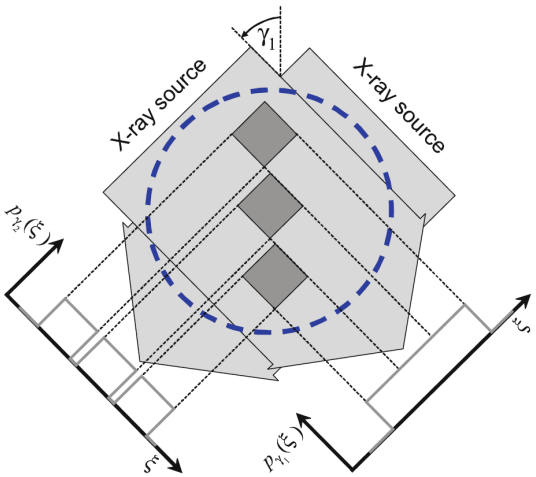

(a) Schematic illustration of one-dimensional X-ray images taken at two different angles γ_1 and γ_2. The three exposed objects have homogeneous intersections. The detector arrays measure the produced X-ray attenuation profiles $p_{\gamma_i}(\xi)$, $i = 1, 2$. The dashed lines indicate the geometric shadow boundaries. In $p_{\gamma_2}(\xi)$, the X-ray attenuation profile shows the correct number of objects while it is not possible to draw this conclusion from $p_{\gamma_1}(\xi)$.

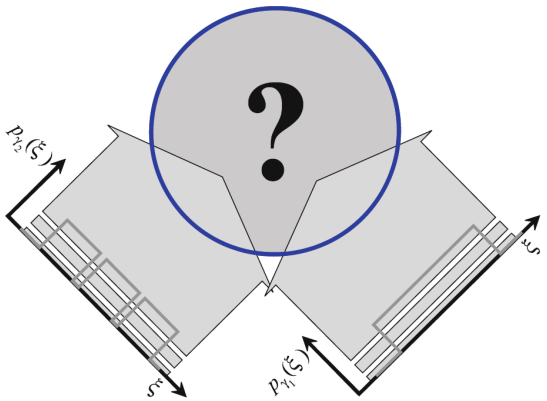

(b) Schematic visualization of the backprojection problem to find the radiodensity map of the scanned object utilizing the one-dimensional X-ray attenuation profiles $p_{\gamma_i}(\xi)$, $i = 1, 2$. The backprojection has to be calculated from a complete set of 180 integral attenuation profiles $p_{\gamma_i}(\xi)$, $i \in \{1, 2, \ldots, 180\}$.

Figure 4.6: Schematics of a) the acquisition of X-ray attenuation profiles of three homogeneous objects in two angles and b) the fundamental backprojection problem in computed tomography.[2]

Equation 4.2. Here, the measured intensity $I(E, s)$ of an ideal detector is divided by the initial intensity $I_0(E)$, logarithmized and multiplied by (-1). As a result, on the right side remains an integral over the irradiated path.

$$-\ln\left(\frac{I(E,s)}{I_0(E)}\right) = \int_0^s \mu(E,x)\rho(x)\mathrm{d}x \tag{4.2}$$

In 1st generation CT, image acquisition is performed by measuring the X-ray attenuation profile along the pixel array of the detector for each projection angle and position of the pencil-beam X-ray source. To link this model description to the physical experiment, a sketch of the data acquisition process of 1st generation CT is shown in Figure 4.7. A total amount of 180 distinct X-ray attenuation profiles in increments of 1° is needed for complete image reconstruction. Calculating the left side of Equation 4.2 for all pixels t along the detector at a specific projection angle Θ gives the intensity profile $p_\Theta(t)$ (Equation 4.3), characterized by the projection angle.

$$p_\Theta(t) = -\ln\left(\frac{I(E,s)}{I_0(E)}\right)(\Theta, t) \tag{4.3}$$

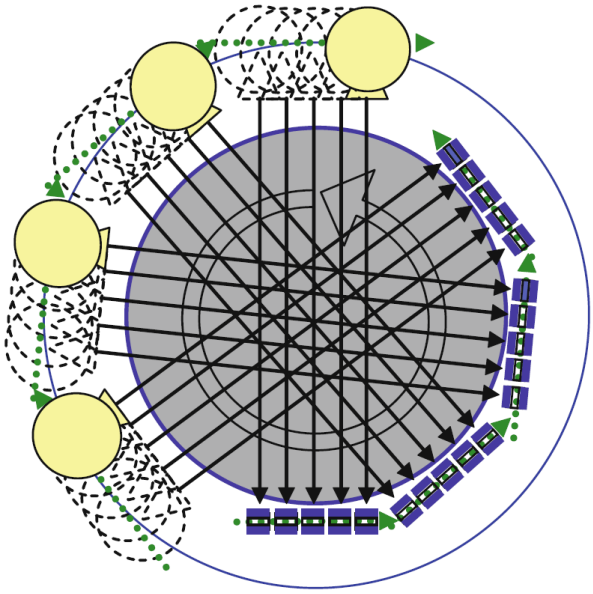

Figure 4.7: Schematic illustration of a 1st generation CT scanning process. The X-ray source and detector rotate around the center. The scanned area is pictured in gray.[2]

The cornerstone in the filtered backprojection method is the Fourier Slice Theorem (FST) which states the relation between the projection $p_\Theta(t)$ of the radiodensity distribution of the scanned object $f(x, y)$ in the spatial domain and its corresponding distribution in the frequency domain $F(u, v)$. According to the Fourier Slice Theorem (see Figure 4.8), the one-dimensional Fourier transform $P_\Theta(\omega)$, with the frequency ω, of the projection profile $p_\Theta(t)$ yields the distribution of $F(u, v)$ along one slice through the origin in the Fourier domain. Hence, $F(u, v)$, the Fourier transform of $f(x, y)$, can be constructed from sufficiently many projections $p_\Theta(t)$. A simple superimposing of all $P_\Theta(\omega)$ would lead to $F(u, v)$ being sampled proportional to $1/|\omega|$. Oversampling is avoided by "filtering" $P_\Theta(\omega)$ by multiplying it with $|\omega|$ (so called Ram-Lak-Filter). The filtered $P_\Theta(\omega)$ is denoted with $Q_\Theta(\omega)$. Only superposition of the $Q_\Theta(\omega)$ leads to the correct $F(u, v)$.

To reduce the level of complexity, in this thesis, the aforementioned FST is employed to replace a two-dimensional inverse Fourier transform of $F(u, v)$ with a one-dimensional one of the $Q_\Theta(\omega)$. In summary, the following four steps are performed, with 1 to 3 illustrated in Figure 4.9:

1. $p_\Theta(t)$ is Fourier transformed (FFT) $\rightarrow P_\Theta(\omega)$
2. $P_\Theta(\omega)$ is filtered with a Ram-Lak-filter: $P_\Theta(\omega) \cdot |\omega| = Q_\Theta(\omega)$
3. $Q_\Theta(\omega)$ is inverse Fourier transformed (IFFT) $\rightarrow q_\Theta(t)$
4. Backprojection of $q_\Theta(t)$

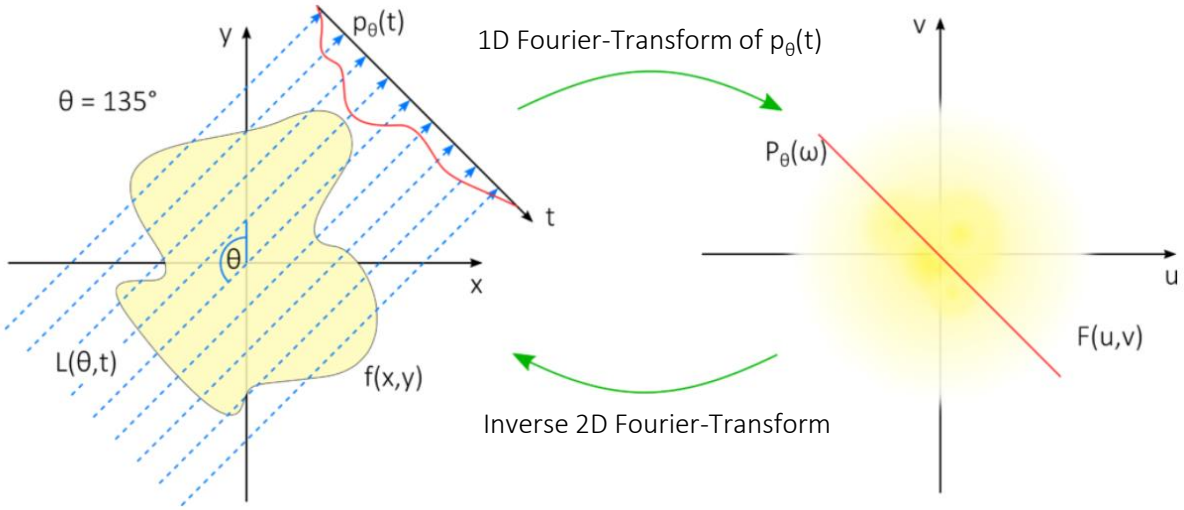

Figure 4.8: Schematic representation of the relation between spatial and frequency (Fourier) domain applied to image reconstruction (Fourier Slice Theorem). The graphic is taken from [30].

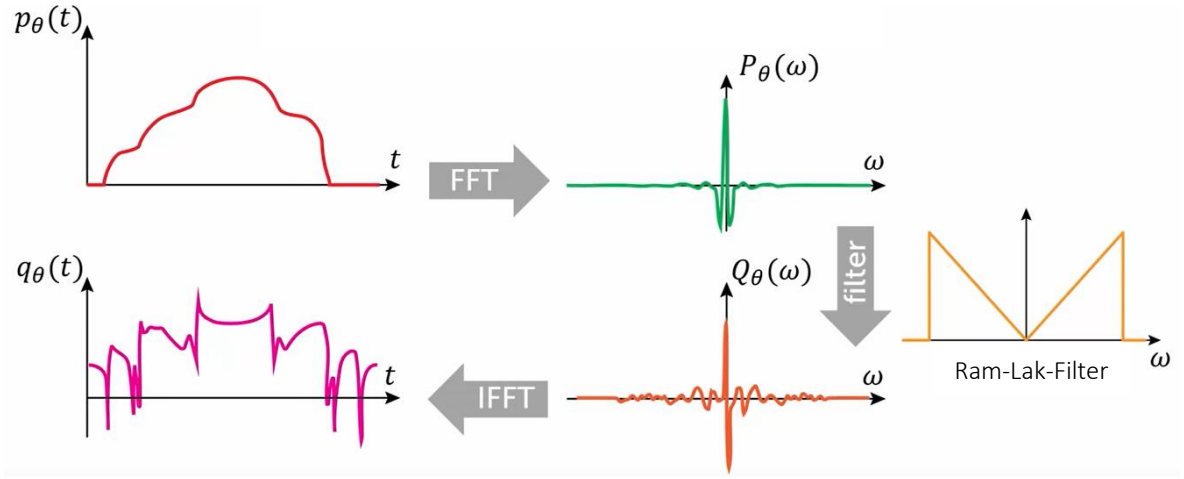

Figure 4.9: Schematic illustration of the filtering of the intensity profiles in the Fourier domain.[31]

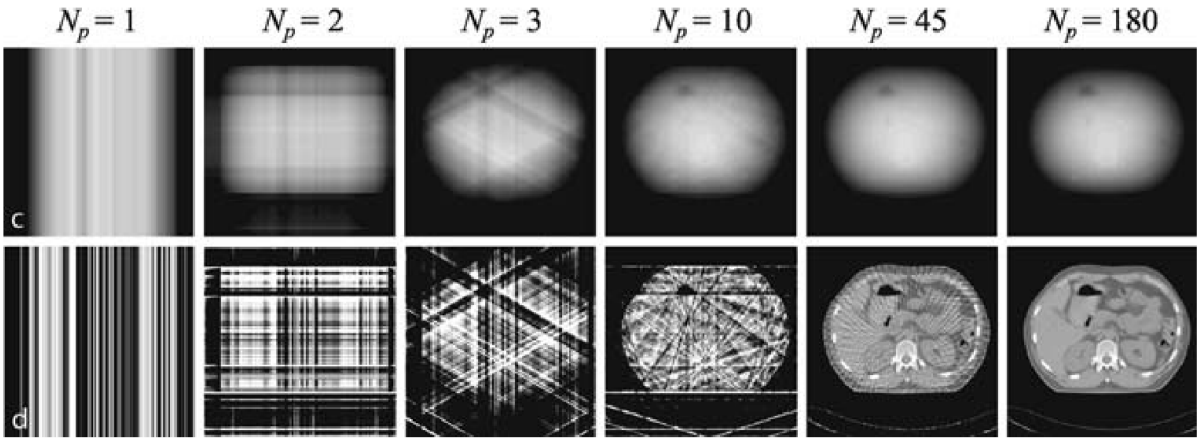

Figure 4.10: An illustration of the effect of increasing iterations for above unfiltered and below filtered backprojection.[2]

In step 4, the actual backprojection is carried out by superimposing the projection data $q_\Theta(t)$ to a reconstruction grid of the size of $f(x, y)$. Repeating this for every individual projection angle yields the final reconstruction of $f(x, y)$. An exemplary evolution of a filtered backprojection with N_p iterations is shown in Figure 4.10 taken from [2]. It is evident, that the backprojection without filtering in the Fourier domain leads to blurry edges, whereas the filtered version leads to more pronounced features. In commercial CTs, filtering the projection data in the Fourier domain also involves additional filter functions[2][30], intended to remove high frequency noise, implement a upper frequency threshold and/or smooth the data.

For better comparability between different measurements, calibration of the reconstructed images is crucial. This is achieved by calibrating the backprojected image to Houndsfield units HU, as introduced in [1]. The HU are calculated via the calibration formula given in Equation 4.4, with μ_w and μ_a being the backprojection values for water and air, respectively.

$$\mathrm{HU} = 1000 \cdot \frac{\mu - \mu_\mathrm{w}}{\mu_\mathrm{w} - \mu_\mathrm{a}} \tag{4.4}$$

Those values are typically determined scanning a calibration phantom with known material and density distribution. The HU scale is defined such that the value for air is -1000 HU and the one for water is 0 HU. Dense materials such as bone have positive values.

4.3 Phantom

The phantom scanned in this thesis consists of extruded Polymethyl methacrylate (PMMA) and is of cylindrical shape. A schematic illustration and photographs of the phantom are shown in Figure 4.11 and Figure 4.12, respectively. The diameter is 30 mm and the height

Atomic number	Mass fraction
Z=1	0.080541
Z=6	0.599846
Z=8	0.319613

Table 4.1: Fraction by weight for different atomic numbers of PMMA $C_5H_8O_2$ [32][33].

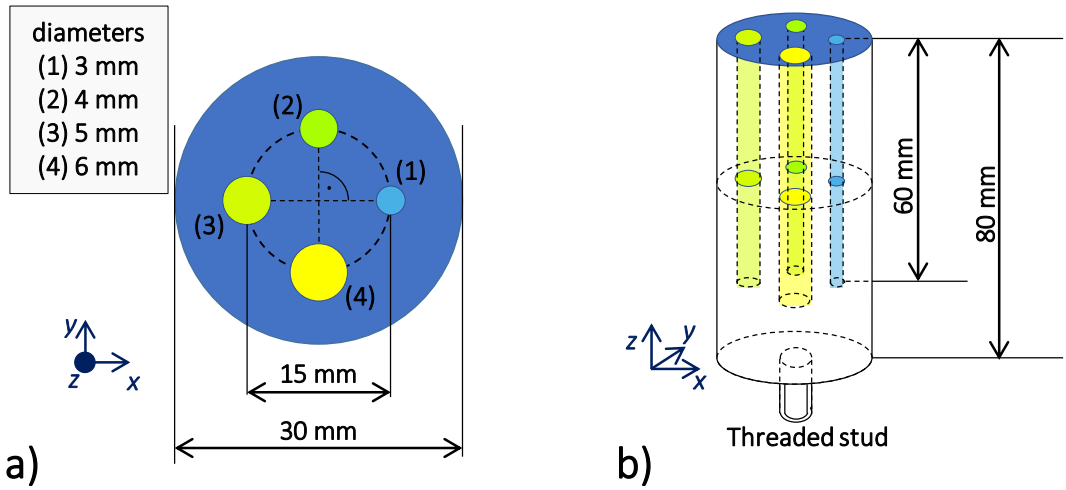

Figure 4.11: Schematic representation of the cylindrical phantom with four drilled holes and a threaded stud. a) top view and b) perspective view. The four drilled holes are arranged with equal distance along a concentric circle of 15 mm.

is 80 mm. The height is orientated on the size of the scanned mouse in [12]. Four cylindrical holes with different diameters and a length of 60 mm are drilled along the z-axis of the PMMA block. PMMA is chosen as basis material due to its lower attenuation coefficient of X-rays in the range of (10–70) keV than H_2O (see Figure 4.13). The photoelectric absorption is the dominant interaction for photon energies up to about 50 keV. For photon energies above that, Compton scattering prevails until pair production is more likely (at energies >10 MeV). The elemental formula for PMMA is $C_5H_8O_2$ [32] with fractions by weight according to Table 4.1. The drilled holes are of different diameters and contain water (H_2O) with different concentrations of molybdenum (Mo, Z = 42 [34]), tabulated in Table 4.2. The liquids were mixed by Johanna Lotter as described in [35]. The photoelectric absorption is the dominant interaction process with molybdenum for photon energies between 10 keV and 70 keV.[19] For molybdenum, the energy of the $K_{\alpha 1}$ radiation is 17.479 keV and of the $K_{\alpha 2}$ radiation is 17.374 keV while the corresponding K-edge is at 20 keV (binding energy for electrons in the K-shell / 1s-orbital).[18] In this thesis, molybdenum serves as contrast medium as well as fluorescent medium in the X-ray measurements, similar to the setup described in [11] and [12]. The publication [36] classifies molybdenum as physiologically important and feasible for X-ray fluorescence imaging.

(a) Side view. (b) Perspective view. (c) Top view.

Figure 4.12: Photos of the cylindrical PMMA phantom with four drilled holes, containing a solution of H_2O with different mass fractions of molybdenum (Mo) (0 %wt, 0.50 %wt, 0.75 %wt, 1.00 %wt).

diameter in mm	3	4	5	6
mass fraction	0 %wt	0.50 %wt	0.75 %wt	1.00 %wt

Table 4.2: Hole diameters and corresponding mass fraction of molybdenum in the water solution.

The purpose of the combination of different concentrations of molybdenum with different diameters of the drill holes in the phantom is advantageous regarding prospective imaging. In the CT image, the sizes of the drill holes are expected to be distinguishable and, consequently, allow for retrospective conclusions about the concentrations according to the diameters of the holes. Furthermore, the hole containing water without molybdenum is supposedly used to calibrate the reconstructed image to Houndsfield units (see section 4.2).

In Figure 4.13, the attenuation coefficients for all material components of the phantom are shown. Additionally, the chosen energy bins for the transmission measurement (chapter 6) are marked in dashed lines, while the red area states the energy bin with the highest inter-material differences in attenuation coefficient, (20–24) keV.

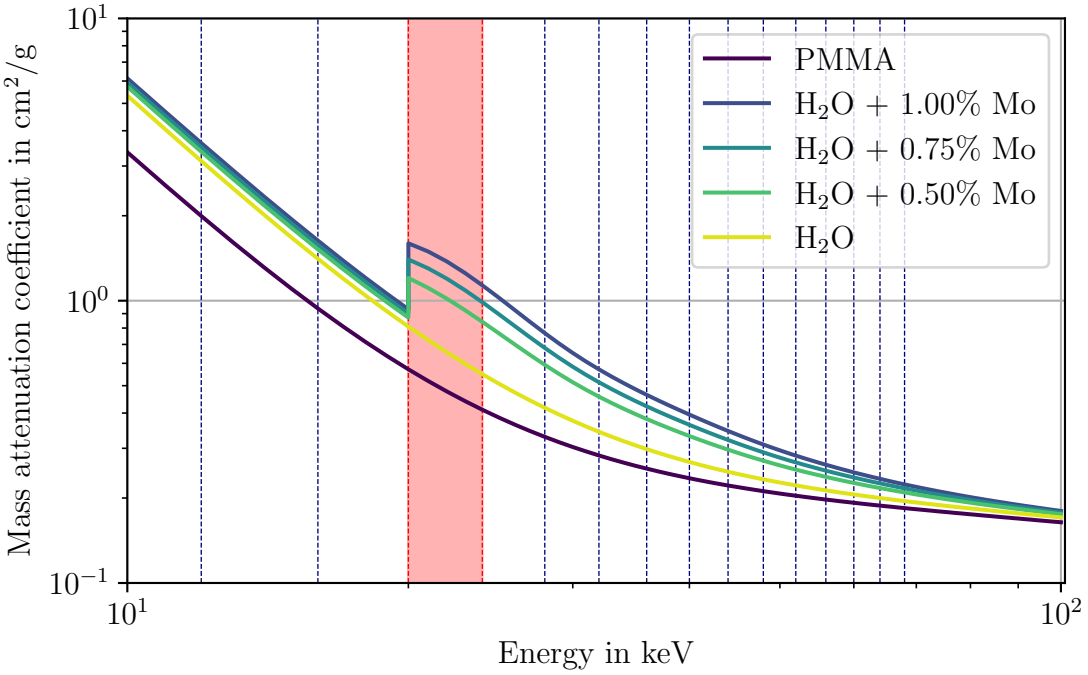

Figure 4.13: Energy dependency of the total attenuation cross section for all material components of the phantom. The fraction of molybdenum is given as a fraction of mass. The vertical lines correspond to the chosen bin edges of the Dosi-mode measurement. The red energy bin is marked due to the highest inter-material differences in attenuation coefficient. The data is taken from [17]

5 Detector Characterization

Contents

The detector used in this thesis is the novel hybrid spectroscopic photon counting pixel detector Dosepix, introduced in section 4.1. Spectroscopic measurements in the true energy scale require an calibration of the internal ToT measured with known photon energies. In this chapter, the energy calibration as well as necessary evaluations are presented.

The energy calibration of Dosepix is carried out utilizing a radioactive source, $^{241}_{95}$Am, in combination with a thin molybdenum sheet of 0.03 µm thickness. The measured data is processed the neural network model described in [9] which returns a parameter prediction for the calibration parameters a, b, c, t for each pixel. The calibration relation between the deposited energy and the measured ToT-value is shown in Equation 5.1. The inversion of this equation yields Equation 5.2 while the lower energy threshold E_{THL} of the measured deposited spectrum corresponds to the energy value assigned to the ToT= 0 (see Equation 5.3).

$$\mathrm{ToT}(E) = aE + b + \frac{c}{E - t} \tag{5.1}$$

$$E(\mathrm{ToT}) = \frac{1}{2a}\left(ta + \mathrm{ToT} - b + \sqrt{(b + ta - \mathrm{ToT})^2 - 4ac}\right) \tag{5.2}$$

$$E_{\mathrm{THL}} = E(0) = \frac{1}{2a}\left(ta - b + \sqrt{(b + ta)^2 - 4ac}\right) \tag{5.3}$$

5.1 Threshold Equalization for Dosepix Detector Pixels

Before starting the calibration measurement, a threshold equalization is mandatory for achieving a nearly equal response characteristic of the pixels. Pixel-to-pixel variations exist due to transistor mismatches and voltage drops along pixel columns, causing differences in the analog threshold of each pixel. To account for these differences, 6-bit registers called pixelDACs are implemented in the pixel electronics to adjust the thresholds of each pixel. This adjustment is performed as described in [25]. Therefore, the detector is placed in

a dark environment with minimized photon exposure. A python script is used to scan the analog threshold from high to low energy and count the number of registered events, i.e., the number of events with signal amplitudes larger than the current threshold value. The noise edge, where the counts surpass the noise count limit, is saved. This scan is conducted at both minimum and maximum pixelDAC values. After the scans, the adjusted pixelDAC value of each pixel is determined by further processing of the mean values of the respective noise edges. For each pixel, the corresponding pixelDAC value is saved in the detector configuration file. The global THL value (global analog threshold voltage), i.e., the V_ThA parameter of the periphery DAC is determined in the next step. Here, the V_ThA value is continuously reduced by 1 until no pixel counts above the noise limit. This value is reduced by 20 as conservative estimate.

With the change from the 3-slots-board to a smaller board with only one Dosepix slot, this equalization routine leads to higher corresponding energies for analog thresholds above 12 keV. The smaller board, further referred to as board allows two ways of connecting Dosepix: one without (w/o) and one with (w/) adapter. For the prospective measurement of this thesis, it is desirable to reach energy thresholds below 10 keV to achieve sufficiently good energy resolution in the range of (10–20) keV in the fluorescence measurements. Therefore, in order to reduce the lower limit of the measured energy deposition spectrum, a different way to determine the global THL threshold from the adjustment distribution is presented. An example for the adjustment distribution is shown in Figure 5.1. The method to determine the analog threshold described above is denoted with method (1) and the method described in the following with method (2). In the second method, the smallest value in the adjustment distribution is subtracted by 20 and set as V_THA to the configuration file. The result of the calibrated relation of ToT value over deposited energy for the large pixels is shown in Figure 5.2 for five calibrations with the same Dosepix, number 38, and different board and equalization combinations. From top to bottom: the 3-slots-board with the original method 1, then the 1-slot-board denoted with B4 without adapter with method 1 and then method 2. Lastly, B4 with adapter and method 1 followed by method 2. The calibration curves of the large pixels show no abnormality in either of the response characteristics. The histogram of the individual pixel threshold values in keV E_{THL} are given in Figure 5.3. The order of board and equalization combinations is the same as in the aforementioned figure showing pixelwise calibration curves. The corresponding mean μ_{THL} and corresponding standard deviation σ_{THL} of the energy threshold E_{THL} for all calibrations is shown in Table 5.1. The settings for I_{krum} are given as well as the according results of the two final utilized board and Dosepix combinations with higher I_{krum}.

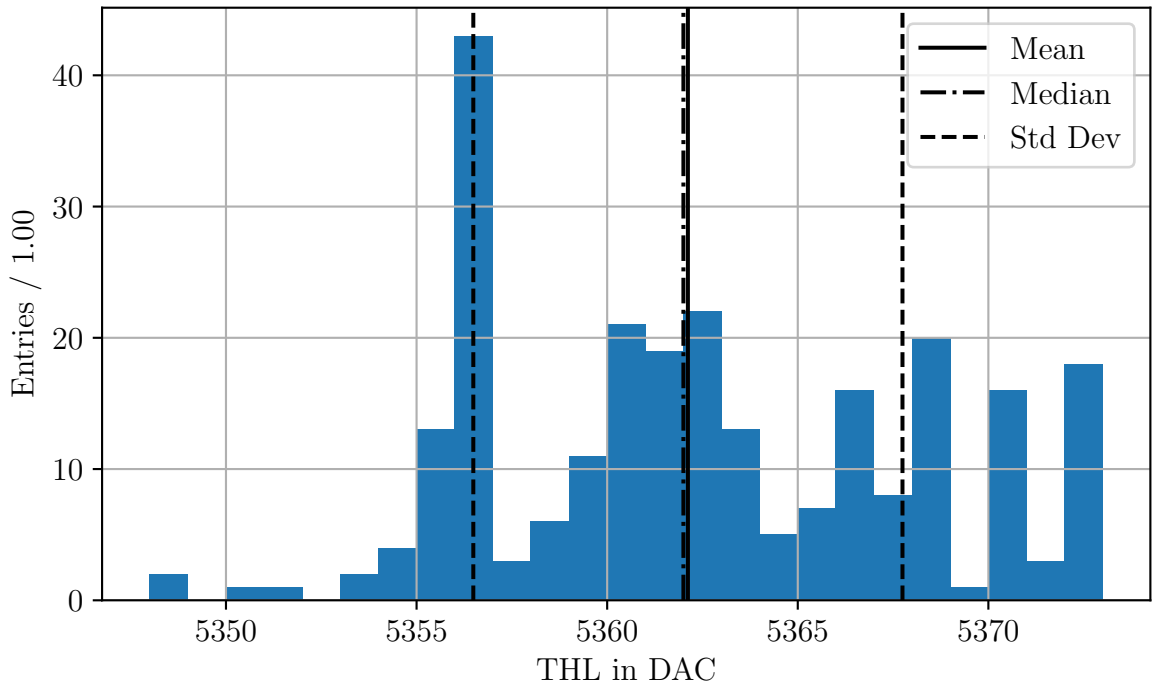

Figure 5.1: Adjustment distribution (histogram of all determined mean values of individual pixel THL values) for board 4, detector 38, w/o adapter. The mean μ_{THL} is 5362 and the standard deviation σ_{THL} is 6 in pixelDACs.

equalization method	board	Dosepix	I_{krum} in nA	μ_{THL} in keV	σ_{THL} in keV
1	3-slots-board	38	2.2	7.6	0.8
1	B4 w/o adapter	38	2.2	11.9	0.6
2	B4 w/o adapter	38	2.2	8.2	0.4
1	B4 w/ adapter	38	2.2	11.1	0.6
2	B4 w/ adapter	38	2.2	8.2	0.3
2	B4 w/ adapter	6	4.4	9.9	0.8
2	B8 w/ adapter	38	4.4	9.0	0.7

Table 5.1: The mean μ_{THL} and corresponding standard deviation σ_{THL} of the energy threshold E_{THL} (after calibration) for the different threshold determination methods: (1) the original one, (2) the alternative presented in this thesis.

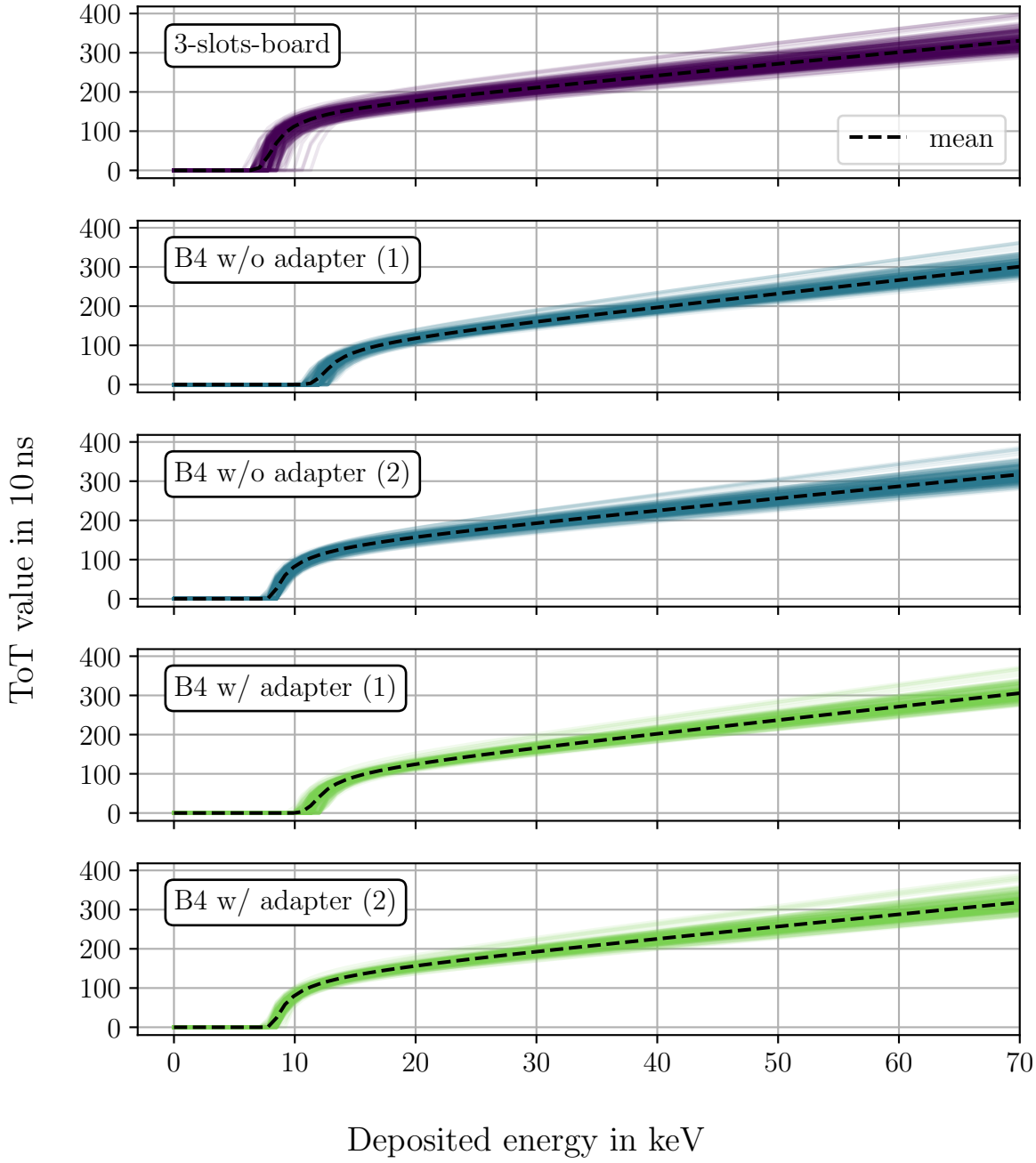

Figure 5.2: Five different calibration curves for detector 38 in combination with different boards (the coloring corresponds to the utilized hardware). The analog threshold V_THA is varied. The number in brackets behind the board type indicates method (1) or method (2) for the derivation of the analog threshold.

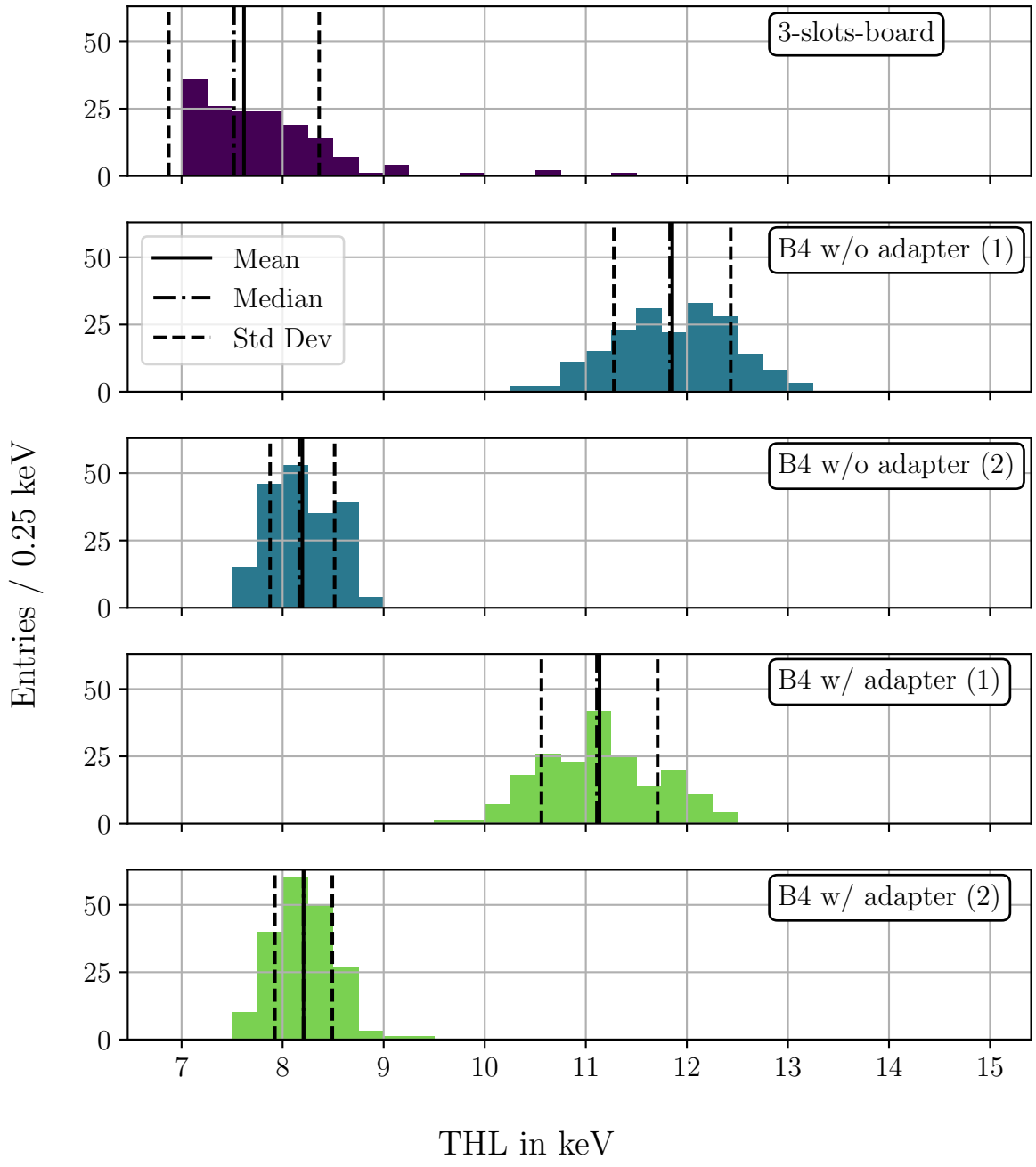

Figure 5.3: Distribution of all pixel energy thresholds E_{THL} of detector 38 in combination with different boards (the coloring corresponds to the utilized hardware). The analog threshold V_THA is varied. The number in brackets behind the board type indicates method (1) or method (2) for the derivation of the analog threshold.

5.2 Energy Calibration via Deep Learning

A calibration measurement in ToT-mode is performed after the equalization of the pixel thresholds. The measurement duration is set to 10 min with minimal frame time of 0.025 s. As introduced at the beginning of this chapter, $^{241}_{95}$Am, a radioactive isotope, is utilized as radiation source for the calibration measurement.[34] It placed in front of the detector with a thin molybdenum sheet of 0.03 µm thickness in between, as shown in Figure 5.4. When the molybdenum sheet is irradiated with gamma rays from $^{241}_{95}$Am, the gamma rays may interact with the atoms in the molybdenum sheet through photoelectric absorption (see section 3.1). This leads to the creation of characteristic X-ray in the molybdenum atoms. The radiation emitted from americium is not fully attenuated in the molybdenum sheet. Hence, both radiations contribute to the measured ToT deposition spectrum. Table 5.2 contains the relevant initial energies and the expected deposited energies of americium and molybdenum. Finally, a neural network described in [9] is utilized to attain a parameter prediction on the calibration parameters in Equation 5.1 for each pixel. In Figure 5.5, the summarized ToT spectra acquired in the calibration measurement over all pixels are shown in a) for both calibrated board-detector combinations. Part b) gives the respective calibrated deposition spectra in keV. Furthermore, the calibration curves for the both board-detector combinations employed in this thesis are presented in Figure 5.6. The resulting mean and standard deviation of the energy threshold distribution is added to Table 5.1.

The difference to the calibration measurements of the previous section is the selected I. The prospective X-ray measurements of this thesis require long exposure times which lead to heat dump in the detector. Hence, the settings need to be chosen to increase

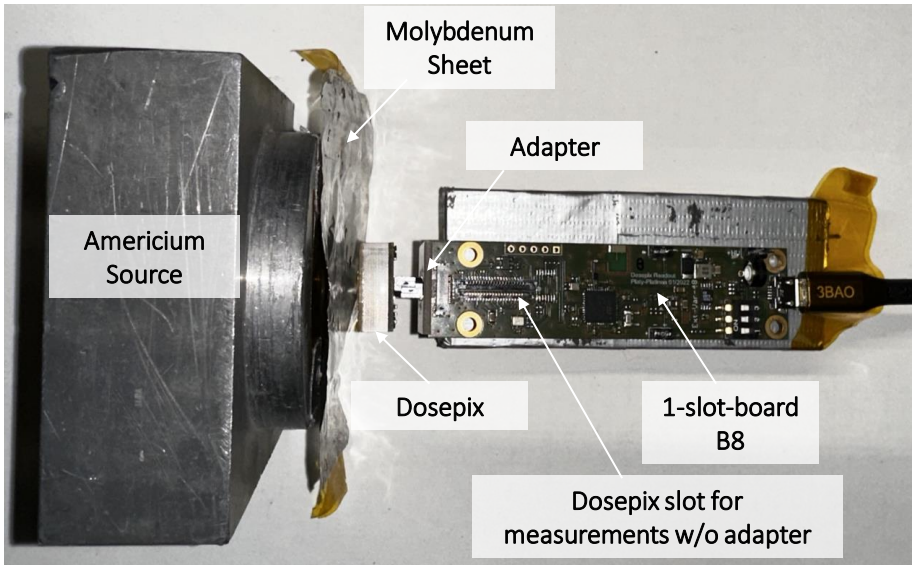

Figure 5.4: Photograph of calibration setup.

source	E_{init} in keV	E_{dep} in keV
Am	59.54	59.35
Mo	17.44	17.27

Table 5.2: Initial energy taken from [34] and deposited energy taken from [9] for americium and molybdenum.

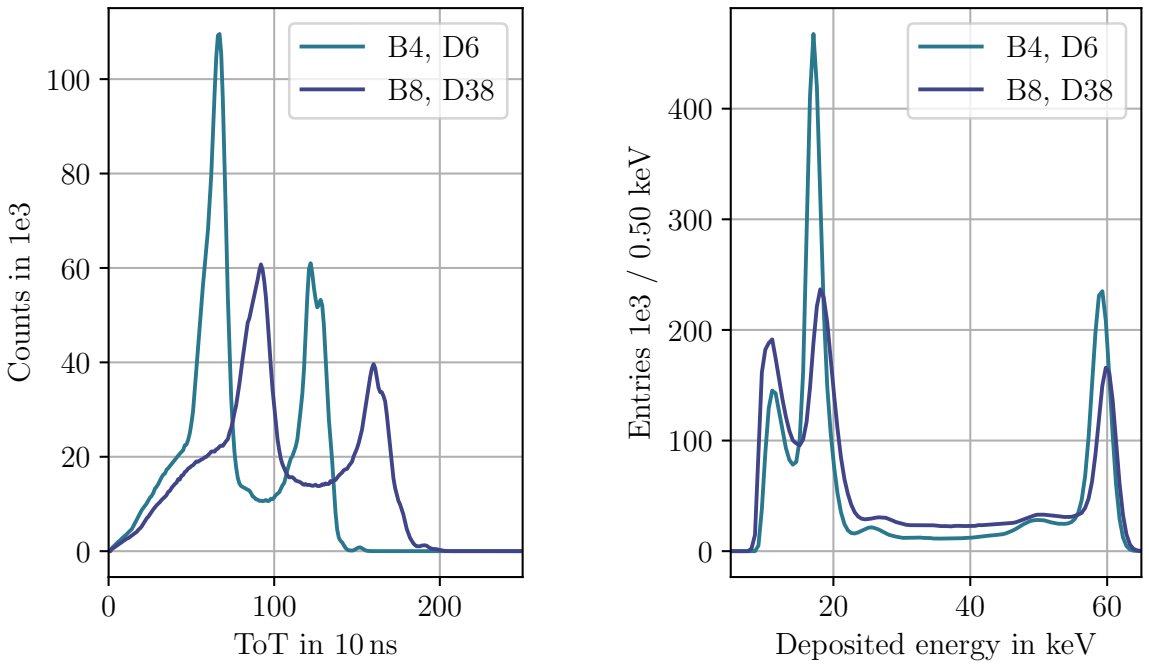

(a) Summarized ToT spectrum before calibration.

(b) Summarized energy deposition spectrum after calibration.

Figure 5.5: Energy deposition spectra before and after calibration for both board-detector combinations employed in this thesis.

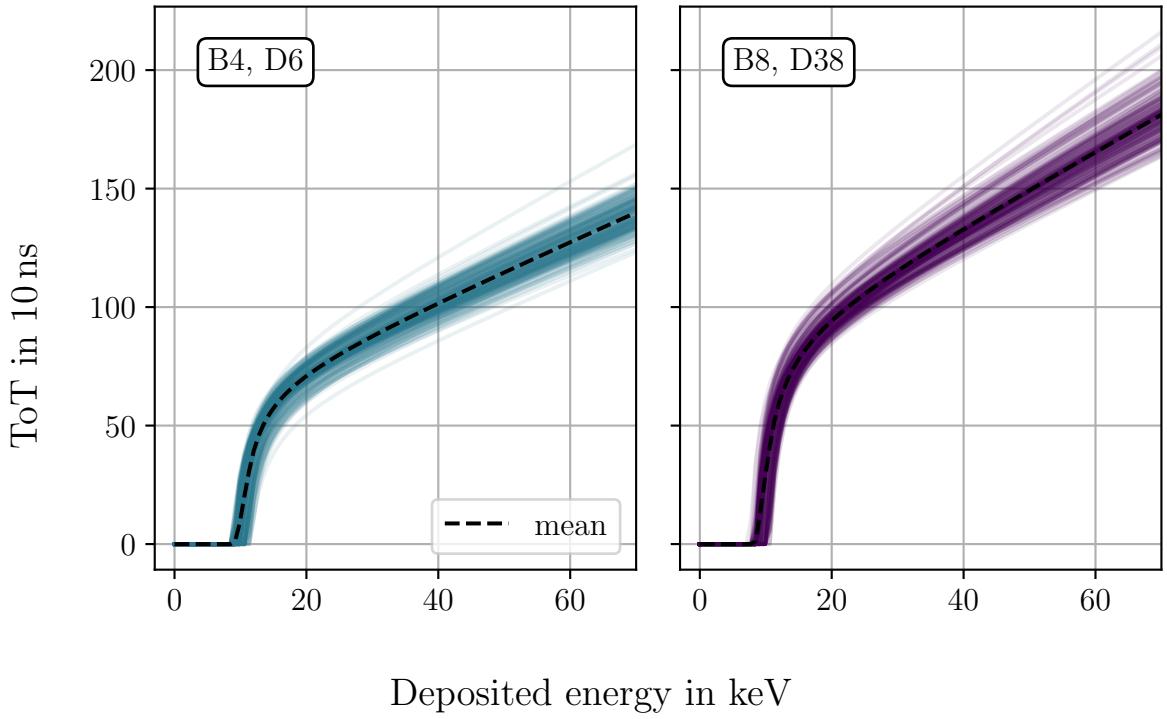

Figure 5.6: Calibration curves for both board-detector combinations employed in this thesis.

temperature stability of the acquired deposition spectra. Temperature fluctuations are one of the main challenges when using the Dosepix detector. Previous theses on the Dosepix detector approach this issue [37][27]. Is is shown that higher I_{krum} reduces the impact of temperature fluctuations.[37] After personal correspondence with Florian Beißer, an I_{krum} of 4.4 nA is set in the measurements underlying this thesis. Furthermore, assuming that the temperature of Dosepix detector reaches an equilibrium state after a certain amount of measurement time, the temperature fluctuations are expected to be lower during longtime measurements.

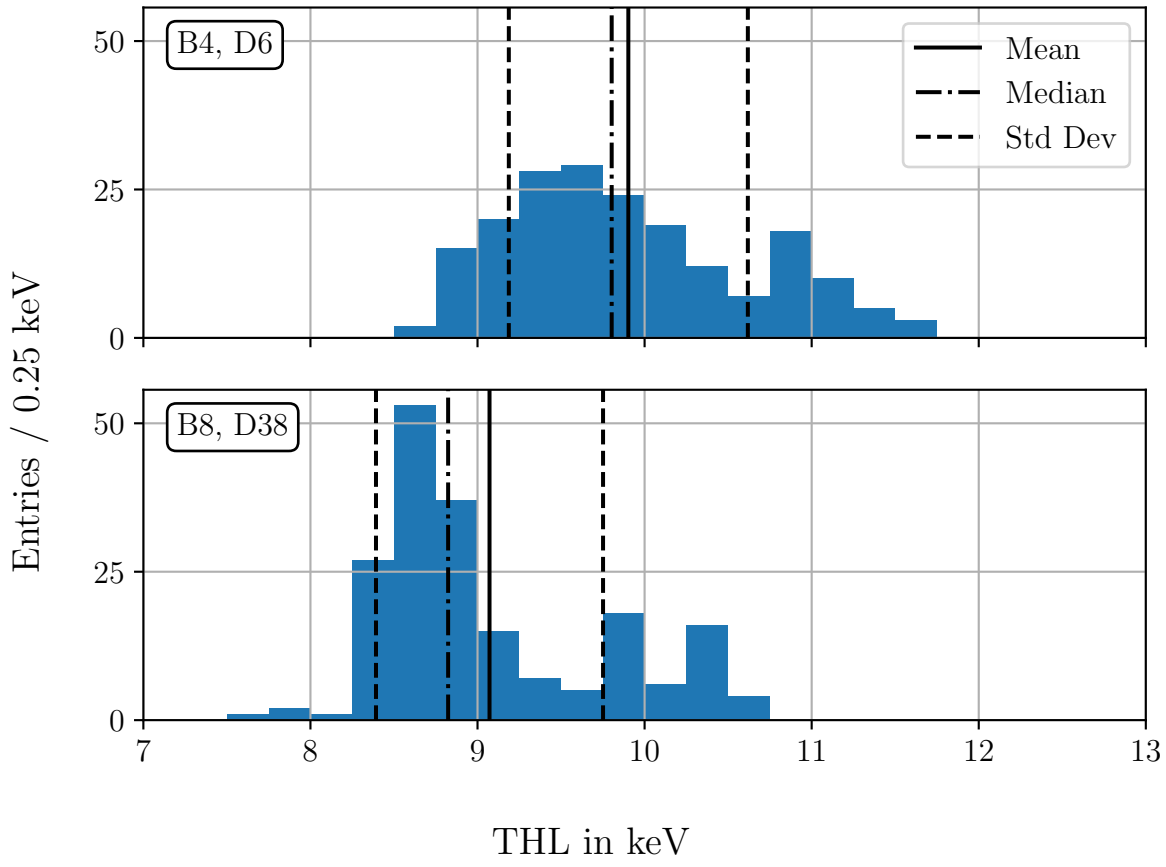

Figure 5.7: Distribution of all pixel energy thresholds E_{THL} for the utilized board-detector combination after the calibration.

6 Computed Tomography with Dosepix

Contents

The Dosepix detector was utilized to perform an XRTCT (X-Ray Transmission Computed Tomography), further referred to as CT, resulting in a radiodensity map of one horizontal slice in the xy-plane of the scanned object (phantom). In this chapter, a detailed description of the experimental setup and data acquisition process employed in the thesis is provided. Following the derivation of X-ray projection lines, a filtered backprojection algorithm is utilized to reconstruct the aforementioned radiodensity map of the scanned phantom, as discussed in section 4.2. Finally, the reconstructed image is analyzed regarding image quality and plausibility.

6.1 Experimental Setup

The phantom used in this thesis has a diameter of 30 mm which is more than ten times wider than the row of 12 large pixels that the sensor of the Dosepix detector utilizes (12 pixels x 220 µm each equals 2.64 mm [8], small pixels are ignored). In Figure 6.6, which is explained in the following section, the discrepancy of size becomes clear. Therefore, the spatial limitation of the detector's pixel arrangement demands a step wise acquisition of the required X-ray attenuation profiles, similar to a 1st generation CT [2]. The cornerstone for the presented experimental setup lies within the phantom which can be moved linearly in y-direction and pivoted in Θ-direction. In contrast, 1st generation CTs are based on translation and rotation of the X-ray tube and detector array (see section 4.2). The

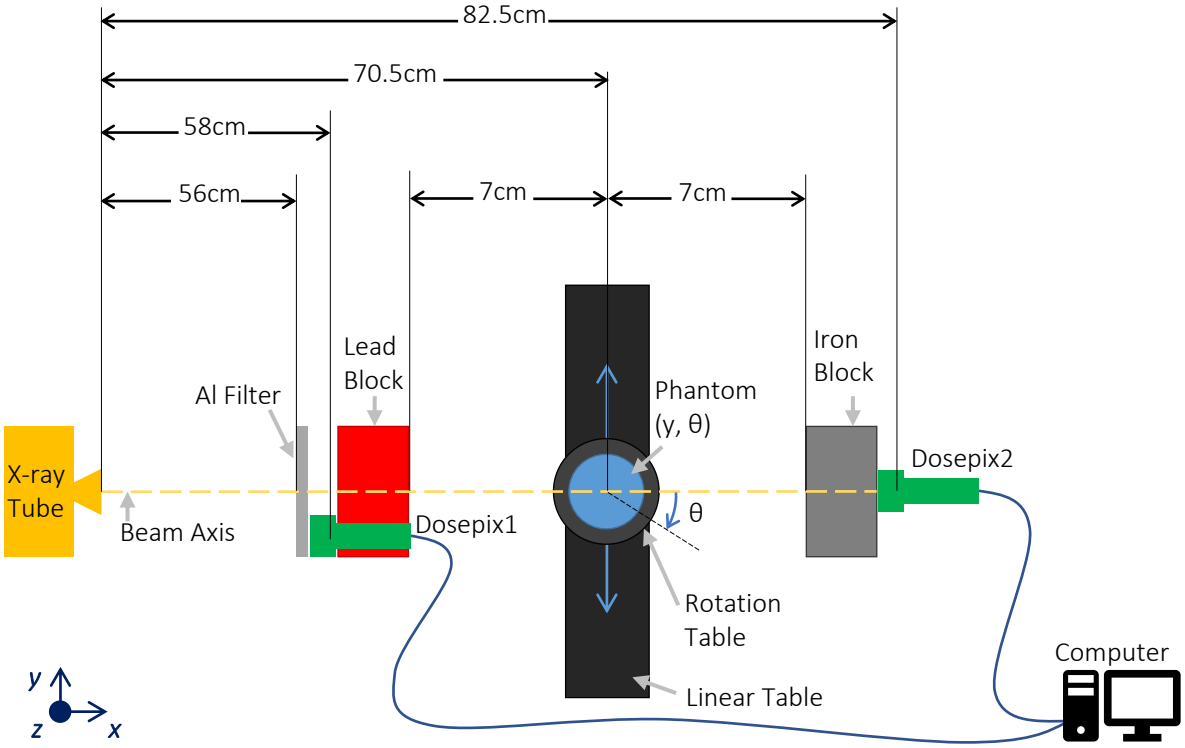

Figure 6.1: Schematic representation of the experimental setup in transmission measurement configuration.

corresponding setup is depicted schematically in Figure 6.1 as well as in photographs in Figure 6.2, and will be explained in the following.

On the most left side of the figure, there is a stationary X-ray source, an X-ray tube with a liquid-metal-jet anode "Liquid-Metal-Jet C2" from Excillum (see section 3.2). For this X-ray tube model, the manufacturer claims a beam width of 10.5° [22]. In order to achieve an approximated pencil beam (in accordance with [15]), two collimators are placed into the beam path to, in sufficiently good approximation, attain a pencil beam and to reduce the impact of scattered photons in the detector denoted with Dosepix2 (board 4, detector 6). The latter is utilized for the acquisition of the X-ray transmission information. Due to availability, a lead and iron block are chosen with 5 cm thickness and holes of 5 mm diameter placed along the beam axis on top of mounting devices. The cylindrical phantom is mounted between the two collimators on a rotational axis which itself is mounted on top of a linear axis. This allows rotation of the phantom around its center axis denoted by the angle Θ and a linear movement perpendicular to the beam along the y-axis of the setup. In this measurement configuration, Θ is commonly referred to as projection angle.

The other detector, denoted with Dosepix1 (board 8, detector 38), is mounted on top of the lead block, facing in direction of the X-ray tube. Dosepix1 is used to monitor the stability, i.e. count rate, of the emitted X-ray spectrum. Both detectors are connected to

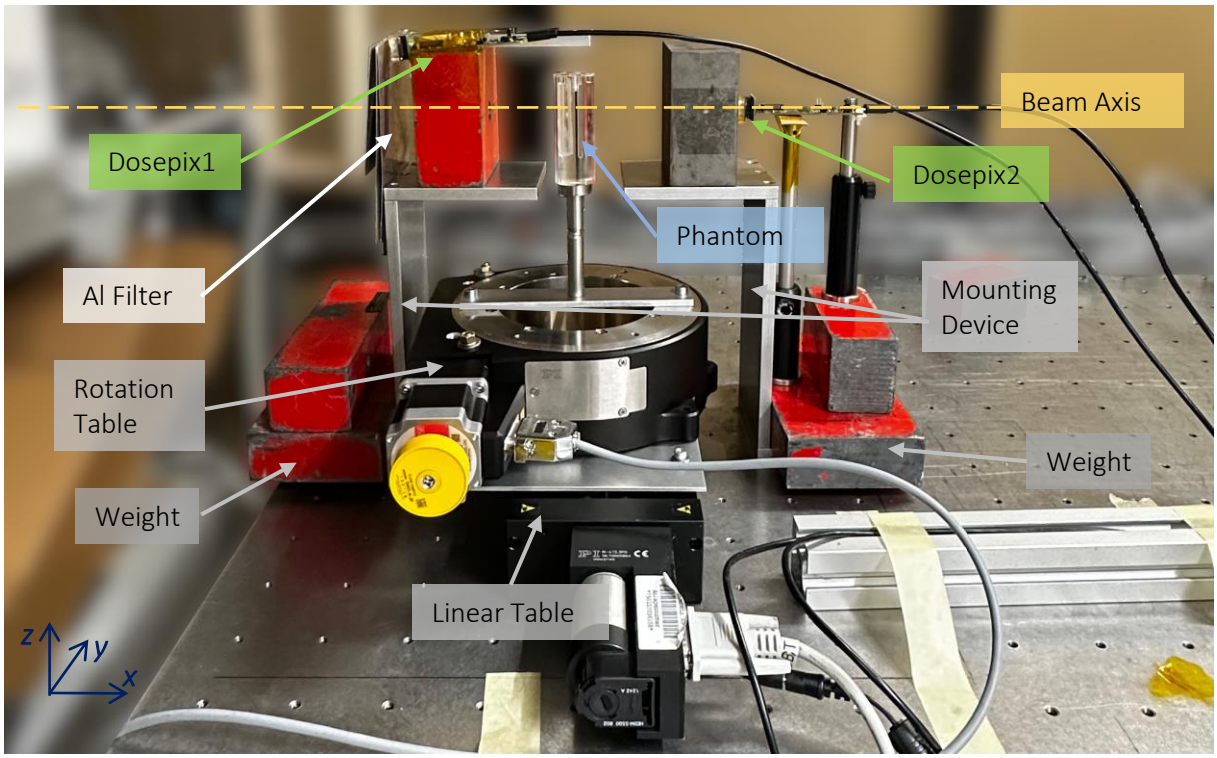

(a) Side view.

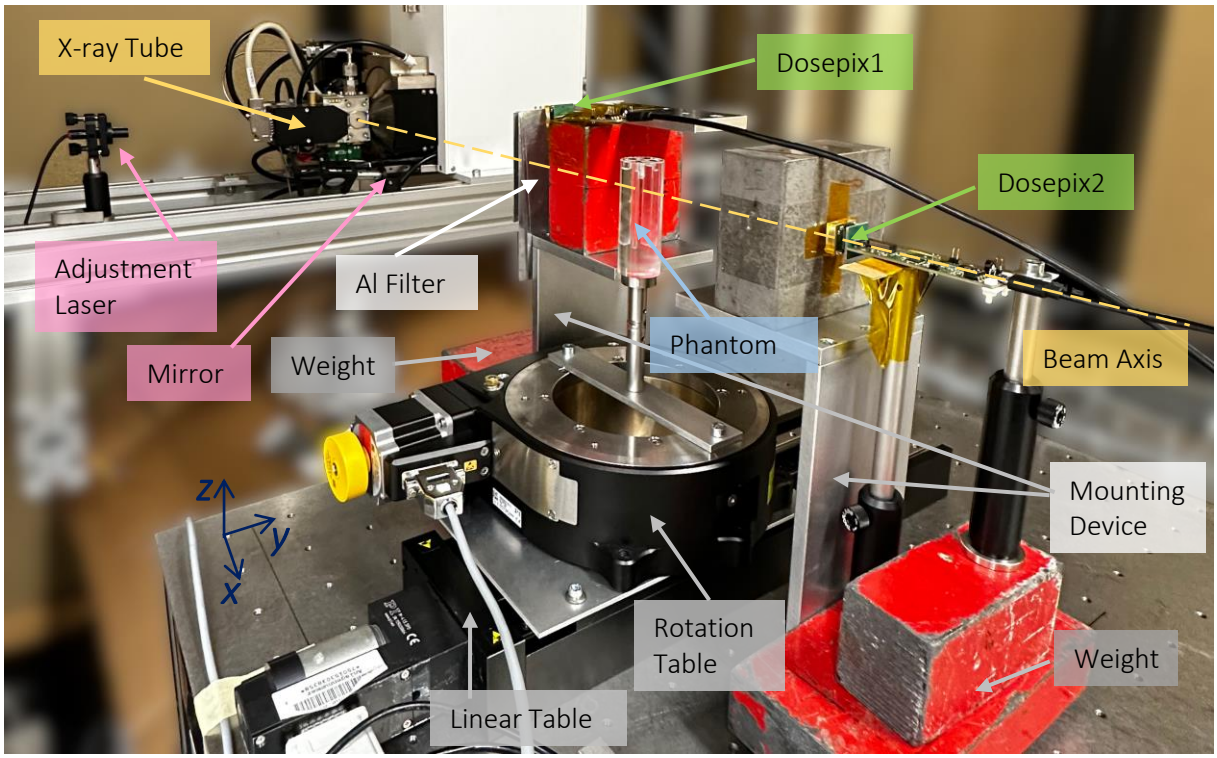

(b) Perspective view.

Figure 6.2: Photos of the X-ray transmission setup from two different views. The side view in a) and the perspective view in b).

Parameter	Value
Voltage	70 kV
Power	50 W
Max. current	0.7143 mA
Min. focal spot size	45 µm

Table 6.1: Settings of the Liquid-Metal-Jet C2 (Excillum) in this thesis.

a computer for data collection and further processing.

One of the major experimental challenges is the emission peak at 9 keV of the spectrum of the X-ray tube. For Dosepix2, the lower threshold of the first energy bin is 10 keV. When photons below the threshold contribute to the Dosepix measurement, then only via pile-up (see section 4.1). This degrades the energy resolution and count rate in the measured energy deposition spectrum, especially in the low energy domain. Consequently, the low energy part of the X-ray spectrum of the LMJ needs to be eliminated. As a solution, an aluminum filter of 5.3 mm thickness is placed into the beam path between X-ray tube and lead block. Filtering the X-ray spectrum with an aluminum filter leads to an overall reduction in photon flux and, more importantly, to so called beam hardening. The latter describes the fact that, according to the Lambert-Beer law (see Equation 3.2), filtering reduces the low energy contributions in the photon spectrum stronger than the high energy contributions. Consequently, the mean photon energy of the beam-hardened X-ray spectrum shifts towards a higher value. The mass attenuation coefficient, taken from [17], and the corresponding transmission in percent for an aluminum filter of 5.3 mm thickness and a density of 2.7 g/cm^3[38] is shown in Figure 6.3.

The setting of the LMJ used for the experiments in this thesis are shown in Table 6.1. There are two possible tube voltages: 30 kV and 70 kV. Due to the filtering with the aluminum filter, 70 kV is chosen in combination with a tube power of 50 W. As explained in section 3.2, the tube voltage yields the maximum photon energy in the X-ray emission spectrum. The tube power of 50 W leads to a sufficiently high photon flux. The minimal focal spot size of 45 µm makes the measurement robust against fluctuations in the focal spot distribution inside the LMJ.

The adjustment laser in combination with the mirror provides a laser beam along the beam axis to ensure proper alignment of the relevant components with the beam axis. It is only applied for the initial installation of the setup. During the measurements, the mirror remains in hinged position and is removed from the beam path.

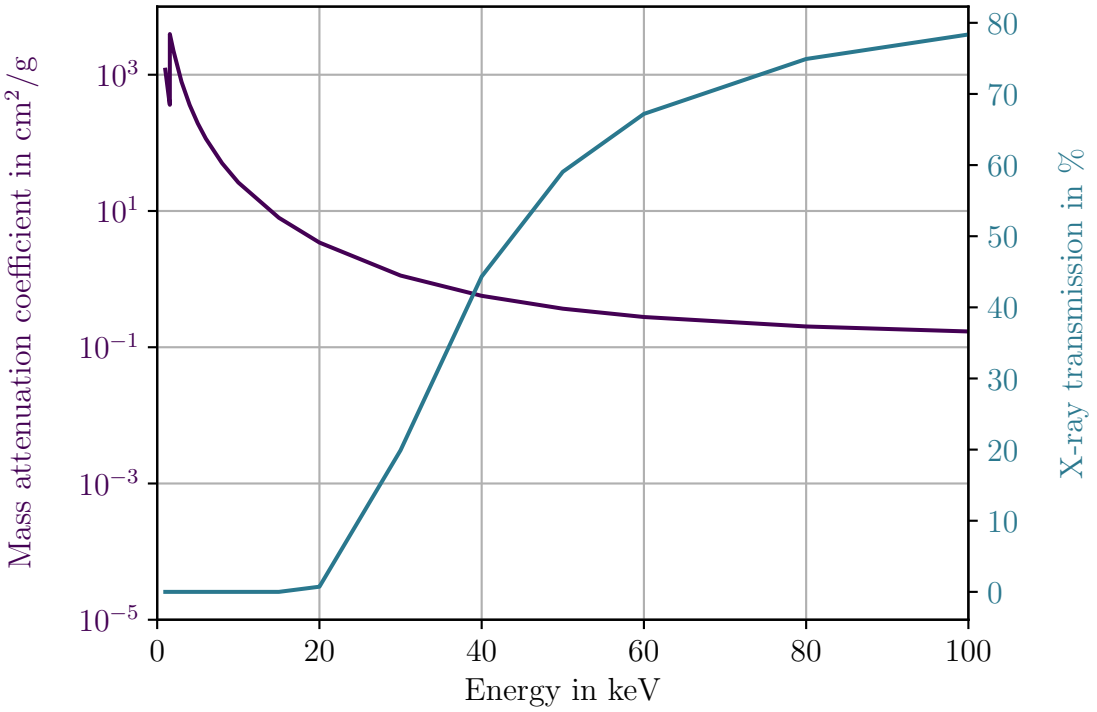

Figure 6.3: Transmission properties of the aluminum filter with 5.3 mm thickness and a density of 2.7 g/cm³.[17][38]

6.2 From Dosepix Measurement to Reconstructed Image

To obtain enough X-ray attenuation information to reconstruct the radiodensity map of a phantom slice, the aforementioned setup is utilized to obtain the required 180 [1] X-ray projections at different projection angles Θ and pixel positions y on the y-axis.

Dosi-mode is utilized for the data acquisition via Dosepix. Each individual measurement at the respective position of the phantom corresponds to a measurement of 7 frames with a frame time of 1 s, therefore, yielding a single measurement time of 7 s. To guarantee synchronized measurements of Dosepix1 and Dosepix2, a total waiting time of 10.5 s is implemented conservatively between each single measurement. In summary, a complete scan takes 23.63 h with a pure acquisition time of 9.45 h. The Dosi-mode acquires pixel wise energy histograms with arbitrarily adjustable energy bin edges. Table 6.2 shows the energy bin edges used for both detectors. The energy bins two to fifteen are equally distributed throughout the emission spectrum of the X-ray source from 12 keV to 68 keV, resulting in a bin width of 4 keV.

As established earlier (section 4.3), the absorption in the third bin ranging from (20–24) keV yields the highest contrast between the materials found in the scanned phantom (see Figure 4.13). Hence, this energy range is chosen in the transmission measurement for the following presentation of the experimental results of the performed CT scan. After

Bin number	Lower energy threshold in keV	Upper energy threshold in keV
1	10.0	12.0
2	12.0	16.0
3	16.0	20.0
4	20.0	24.0
5	24.0	28.0
6	28.0	32.0
7	32.0	36.0
8	36.0	40.0
9	40.0	44.0
10	44.0	48.0
11	48.0	52.0
12	52.0	56.0
13	56.0	60.0
14	60.0	64.0
15	64.0	68.0
16	68.0	

Table 6.2: Chosen energy bins for the X-ray transmission measurement for Dosepix1 and Dosepix2.

selecting the desired energy bin, the entries for each pixel are summed up over all measured frames of the respective measurement. As for the step wise scanning of all X-ray projections, the individually measured transmitted intensity matrices $G_\Theta(y_\mathrm{n})$ are characterized by the projection angle Θ and the n^{th} increment of the phantom position along the y-axis. The projection angle Θ ranges from 0° to 179° in increments of 1° and the step size along the y-axis is chosen to be 1.32 mm corresponding to the edge length of 6 large pixels (half the length of a row of twelve large pixels) in the sensor of the Dosepix detector. Consequently, n is in the range $[1, 27]$.

The measurement time of 7 s per phantom position is sufficient to obtain a minimum of 76 entries in each large pixel. A histogram of the appearance of counts in the original measured $G_\Theta(y_\mathrm{n})$ in the energy range (20–24) keV is shown in Figure 6.4.

Further, fixed-pattern noise in the pixel matrix is reduced performing a flat-field correction as described in [39]. Exemplary plots of the pixel matrices $G_\Theta(y_\mathrm{n})$ obtained in the first five and last five consecutives of n and for the rotation angle $\Theta = 0°$ are shown in Figure 6.5. The values in the matrix are the number of registered events in the chosen energy bin (20–24) keV. The phantom is moved step wise to the left into the beam path (a) and out of the beam path (b). Due to the attenuation in the phantom, the number of registered events decreases when it is moved into the beam path.

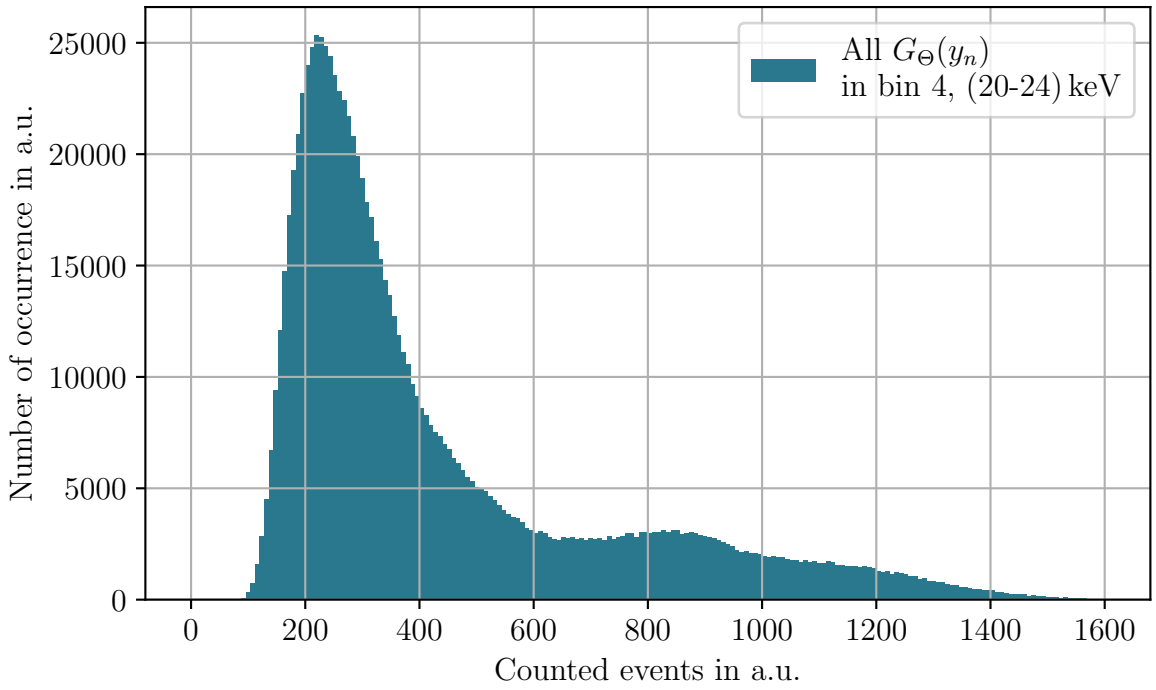

Figure 6.4: Appearance of counts in all $G_\Theta(y_\mathrm{n})$ measured with Dosepix2 in the energy range (20–24) keV without normalization to the count rate obtained with Dosepix1.

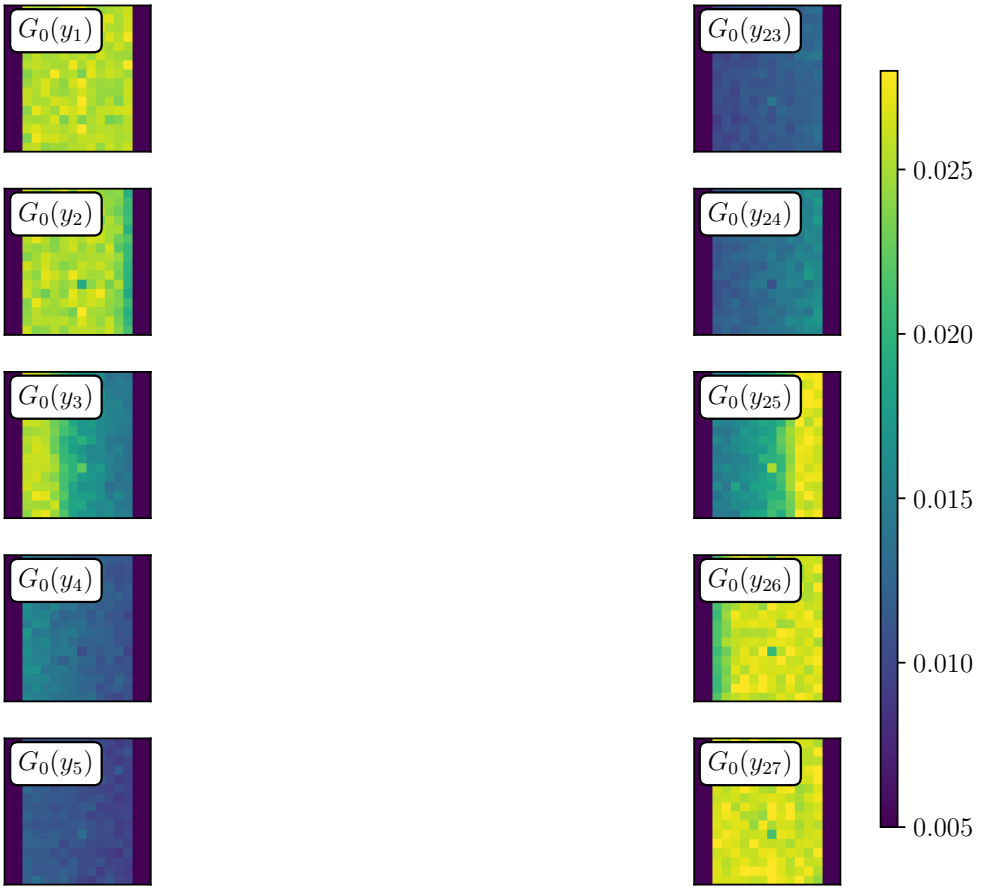

(a) In $G_0(y_1)$, the phantom is not yet in the beam path, all that can be seen is background in yellow. In $G_0(y_2)$, the darker color in the right column indicates that the phantom is partly in the scanned beam path. For $n = 3$ to $n = 5$, the phantom shields the detector more and more, because of the increasing thickness of material in the beam path. The gradual change in blue color within the matrix from left to right is a result of the increasing thickness of the horizontal phantom slice due to its cylindrical shape.

(b) In $G_0(y_{23})$, the phantom is fully in the beam path. For $n = 25$ to $n = 27$, more and more background is scanned because the phantom gradually leaves the beam path.

Figure 6.5: Exemplary plot of the registered number of events in the range (20–24) keV, plotted for each pixel in the pixel matrix $G_\Theta(y_n)$ of the sensor of Dosepix2. In a), the first five ($n \in \{1, 2, 3, 4, 5\}$) and, in b), the last five ($n \in \{23, 24, 25, 26, 27\}$) phantom positions for projection angle $\Theta = 0°$ are shown. The orientation of the pixel matrices is similar to looking at the detector surface in x-direction of the setup. The dark pixels framing the columns to each side of the pixel matrices are deactivated small pixels. The brighter the color, the higher the transmission along the beam path (i.e. background appears yellow) and the darker the color the lower transmission in the beam path (i.e. phantom appears in shades of blue depending on the irradiated thickness).

6.2.1 Derivation of X-Ray Transmission Profiles

As described above, each measurement leads to a transmission matrix $G_\Theta(y_\mathrm{n})$. As the filtered backprojection is applied to each slice of the phantom individually, choosing a row to proceed with the data processing is crucial. Here, the bottom row of the pixel matrices over all individual measurements is selected and denoted with $g_\Theta(y_\mathrm{n})$. Furthermore, the entry in the m^{th} pixel, $m \in [1, 12]$, along the respective row is identified by the pixel ID $g_\Theta(y_{\mathrm{n,m}})$.

Due to the experimental design of moving the phantom half the length of a row of large pixels, the pixels $g_\Theta(y_{\mathrm{n,6+s}})$ and $g_\Theta(y_{\mathrm{n\text{-}1,s}})$, with shifting variable $s \in \{1, 2, 3, 4, 5, 6\}$ and $n \in [2, n_{\max} - 1]$, scan the same part of the phantom. Ergo, a so-called pixel fusion is carried out to determine $g_\Theta(y)$ by averaging over the entries in all $g_\Theta(y_{\mathrm{n,6+s}})$ and $g_\Theta(y_{\mathrm{n\text{-}1,s}})$ with $n \in [2, n_{\max} - 1]$. The limitation for n ensures choosing only twofold measured phantom transmission data. The advantage of this step size is that the measured intensity is less prone to fluctuations in the actual step size provided by the linear table moving the object. This is illustrated in the schematic in Figure 6.6.

6.2.2 Calculation of X-Ray Projection Profiles

In the next step, the integral X-ray projection profiles $p_\Theta(y)$ are calculated via Equation 4.3 from the intensities $g_\Theta(y)$. As explained above, $g_\Theta(y)$ are the pixel entries in the respective chosen row of the detector that scanned the horizontal phantom slice. Hence, $g_\Theta(y)$ is identified with $I(E, s)$. Neglecting the attenuation of X-ray in air, the measured intensity in the background of the phantom $g_{\mathrm{bg},\Theta}$ is the corresponding $I_0(E)$. For $g_{\mathrm{bg},\Theta}$ the mean value over the first ten background pixels of each projection angle is calculated. Thus, negative natural logarithm of the ratio $g_\Theta(y)$ and the background $g_{\mathrm{bg},\Theta}$ yields the integral X-ray projection profiles $p_\Theta(y)$. The pixel values of $g_0(y_\mathrm{n})$, the resulting $g_0(y)$ and the corresponding $p_0(y)$ are shown in Figure 6.7.

After applying the introduced process to all measured phantom angles, exemplary resulting X-ray projection profiles are shown in Figure 6.8. The coloring emphasizes the height of the respective $p_\Theta(y)$ and does not contain additional information.

Stacking all X-ray projection profiles yields the sinogram shown in Figure 6.9. Due to the rotation symmetry of the cylindrical PMMA phantom, the borders of the phantom appear as straight lines, whereas the locations of the drilled holes containing the contrast medium shift with the rotation angle Θ. The drill hole containing water is not visible in the sinogram.

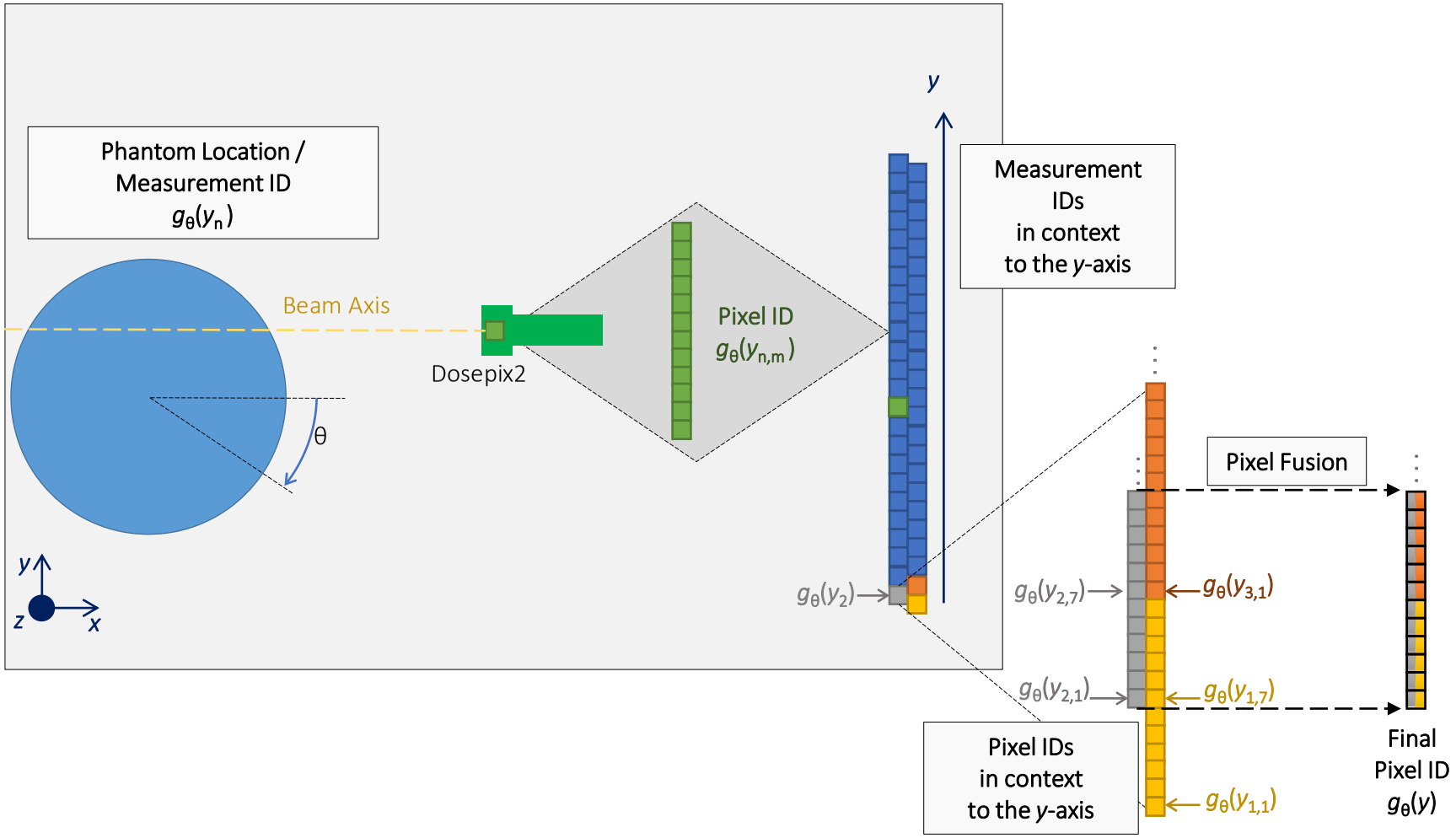

Figure 6.6: Schematic of the generation of the X-ray projection lines along one phantom slice. From left to right: A measurement ID $g_\Theta(y_n)$, is assigned to each measurement according to the n^{th} increment along the y-axis characterized by the projection angle Θ of the phantom. In each measurement, the respective part of the phantom is scanned and consists of 12 pixels along the respective row in the Dosepix sensor. Hence, the pixels are identified by the Pixel ID $g_\Theta(y_{n,m})$ with the additional pixel position index m. All measurement IDs are brought into context along the y-axis considering the step size of 6 pixels (1.32 mm), which is half of the sensor edge length, considering large pixels only. On the right of the schematic, the pixel fusion is explained figuratively. Due to the chosen step size, the pixels $g_\Theta(y_{n,6+s})$ and $g_\Theta(y_{n-1,s})$, with shifting variable $s \in \{1,2,3,4,5,6\}$, scan the same part of the phantom. The mean over the two respective overlapping pixels is calculated and identified with the final pixel ID $g_\Theta(y)$ for the y^{th} pixel along the y-axis.

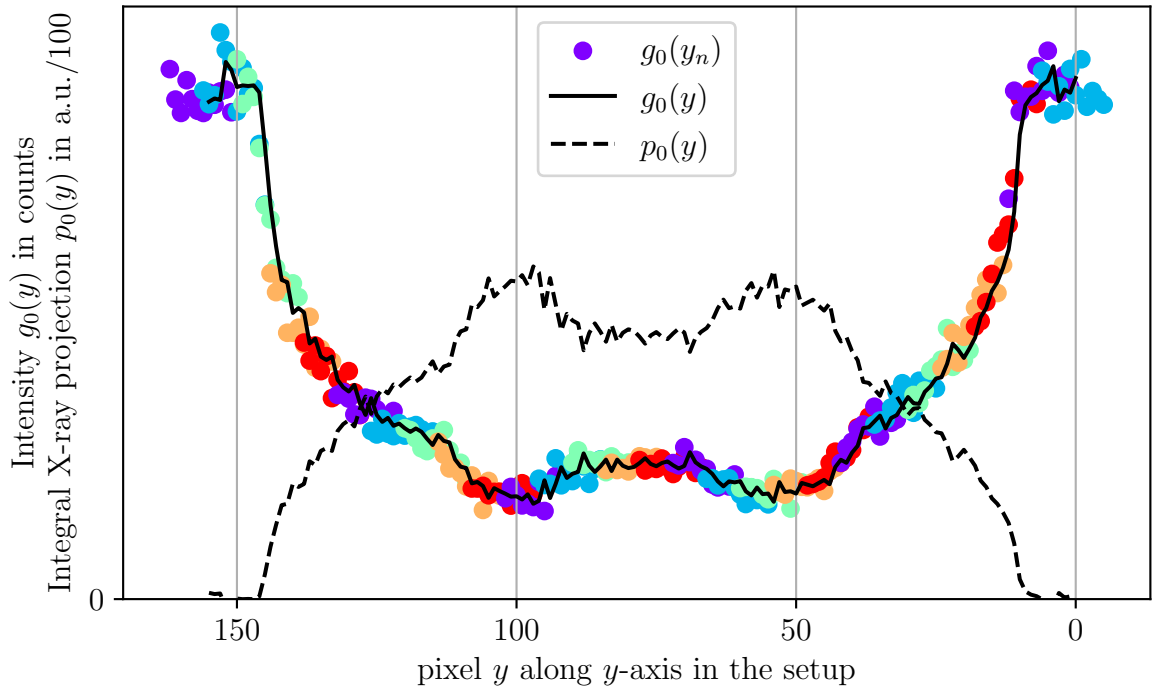

Figure 6.7: The values of the lowest rows of big pixels $g_\Theta(y_n)$ in the pixel matrices plotted over the according pixel on the y-axis in the setup according to the phantom position during one projection angle $\Theta = 0°$. The coloring indicates the different phantom positions n. The resulting $g_0(y)$ and the corresponding $p_0(y)$ are plotted in black.

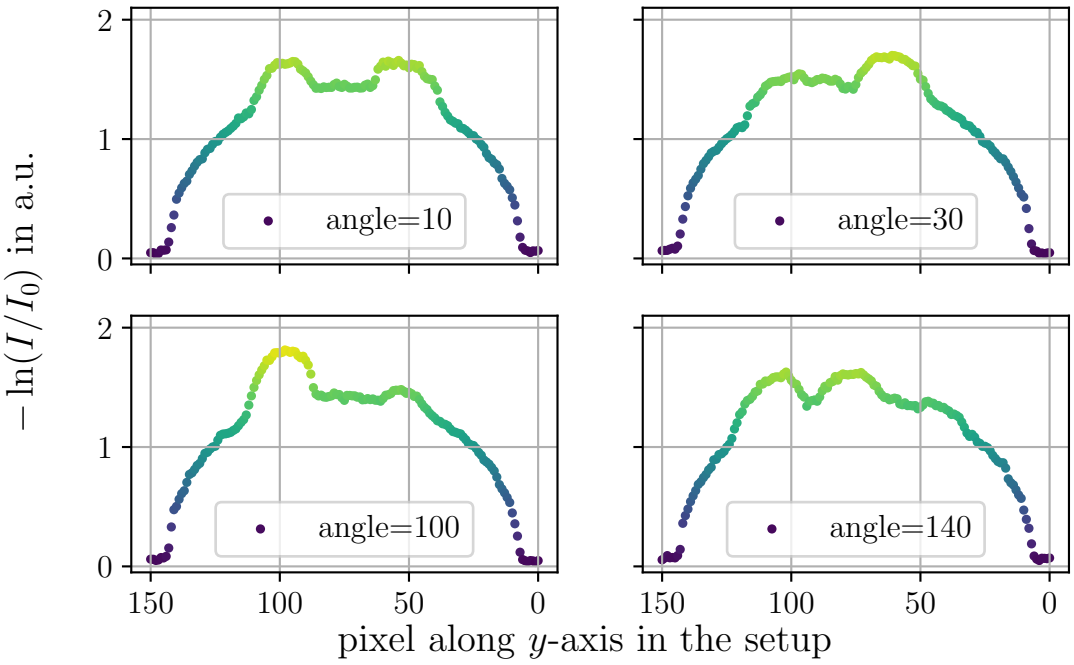

Figure 6.8: Exemplary integral X-ray projection profiles $p_\Theta(y)$ for four different phantom angles Θ. The color of the data points emphasizes the respective value of $p_\Theta(y)$ and does not contain additional information.

6.2.3 Image Reconstruction via Filtered Backprojection

Subsequently a filtered backprojection is performed, utilizing the sinogram as described in section 4.2. A visualization of the iterations of the final backprojection is shown in Figure 6.12. The different images illustrate the 1^{st}, 10^{th}, 45^{th} and 180^{th} iteration of the backprojection process after the filtering. In the first iteration step, the backprojection for only one filtered projection line is superimposed to an empty canvas. In each iteration step, the next filtered projection profile is superimposed to the canvas according to the projection angle. The pixel values μ of the reconstructed image are calibrated to Houndsfield units HU by applying Equation 4.4 from section 4.2. Therefore, the backprojection value of μ_{w} and of air μ_{a} are required. Hence, the reconstructed image is sectioned into different areas identified with different materials of the phantom by applying binary masks to the data. An illustration of the different sections is shown in Figure 6.11 with the background in a), phantom in b), the PMMA body of the phantom in c) and in d) the four drill holes. The drill hole containing only water is not visible in the reconstructed image. Hence, its location is estimated by considering the basic geometry of the phantom, as indicated by the white lines in part b) of the aforementioned figure. The spatial resolution of the reconstructed image is calculated to be (4.53 ± 0.07) pixel/mm by dividing the diameter of

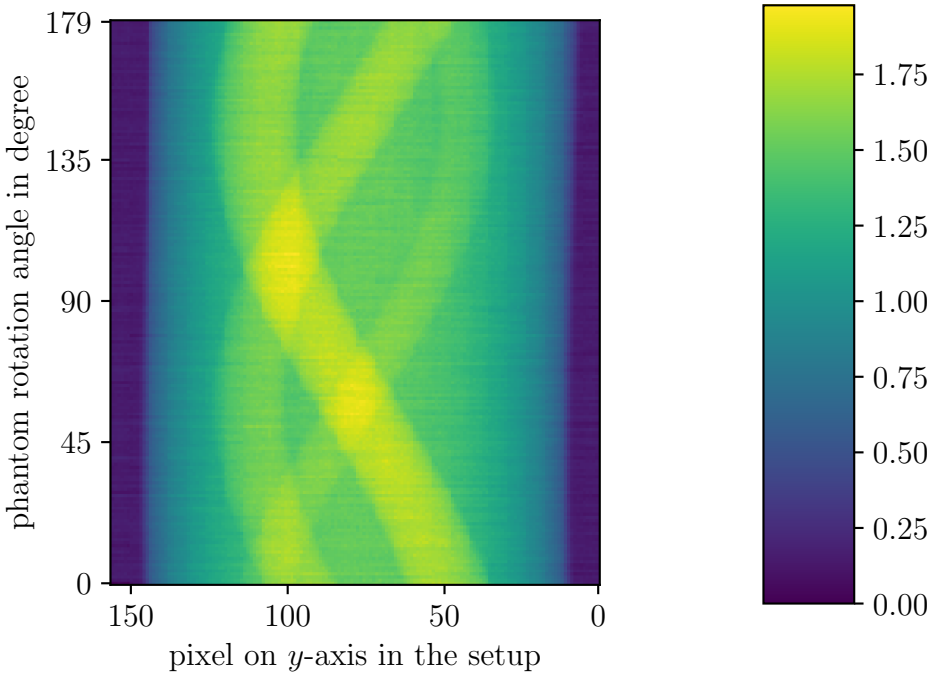

Figure 6.9: Sinogram of the PMMA phantom with contrast medium for the energy range 20–24 keV. The brighter the color, the lower the transmission in the irradiated beam path. Hence, the background is in dark blue. The yellow lines correspond to the location of the drilled holes in the phantom, filled with different concentrations of molybdenum.

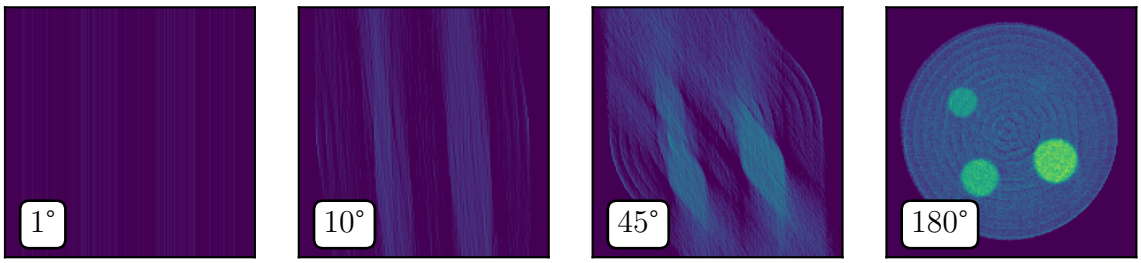

Figure 6.10: The four different images illustrate the 1st, 10th, 45th and 180th iteration of the backprojection process after the filtering. The resulting reconstructed image is the superposition of all filtered X-ray projection profiles.

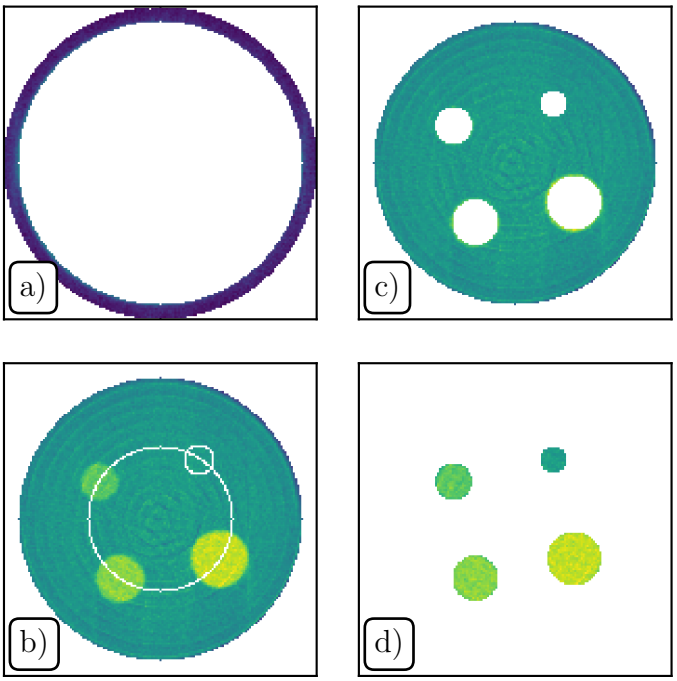

Figure 6.11: Sections of the uncalibrated reconstructed image with a) background, b) phantom with markings for the concentric circle of the centers of the holes and the estimation of the water hole, c) the PMMA part of the phantom and d) the four holes.

the phantom in the reconstructed image (136 pixels) by its real size, 30 mm. The error of the spatial resolution was derived using Gaussian error propagation, where the error of the real phantom diameter is estimated to be 0.1 mm, and for the reconstructed image to be 2 pixels. Table 6.3 gives an overview over all relevant parameters obtained from the reconstructed image. The calibrated reconstructed image is shown in Figure 6.12. The drill holes containing the different concentrations of molybdenum are colored in different shades of yellow. The PMMA body material of the phantom is of a light blue color while the background is imaged in dark blue. The reconstructed image has ringlike artifacts. According to [2], ringlike artifacts originate from pixel differences. This requires further investigation because from the current experimental results, it is not possible to conclude to the exact origin of these artifacts.

Material	Mean over pixels in a.u.	Mean over pixels in HU	Est. diameter in pixels	Calc. diameter in mm
Air	1.247 ± 0.014	-1000 ± 13	-	-
PMMA	5.252 ± 0.005	-84 ± 7	136 ± 2	30.0 ± 0.1
Mo 0%wt	5.62 ± 0.026	0 ± 6	13 ± 2	3.0 ± 0.1
Mo 0.5%wt	7.35 ± 0.026	397 ± 4	18 ± 2	4.0 ± 0.5
Mo 0.75%wt	8.194 ± 0.018	590 ± 4	22 ± 2	4.9 ± 0.5
Mo 1%wt	9.027 ± 0.015	781 ± 3	26 ± 2	5.8 ± 0.5

Table 6.3: Properties of the reconstructed image according to the respective area in the image, named by the respective material in the scanned phantom. Est. stands for estimated, calc. stands for calculated, while for PMMA and water (Mo 0%wt), the diameter in pixels is the calculated one.

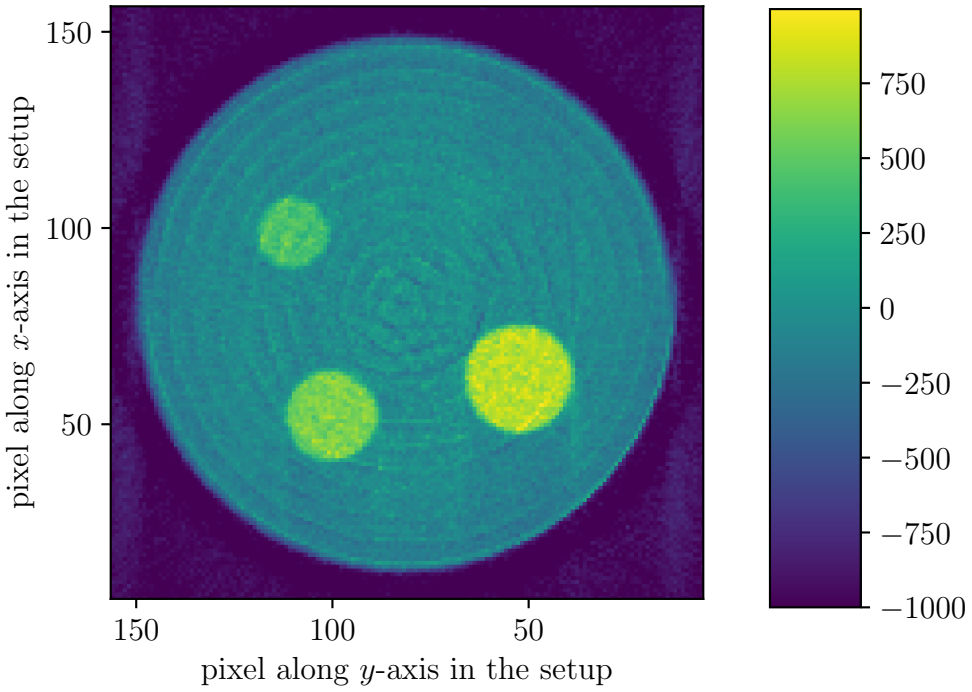

Figure 6.12: The reconstructed image calibrated to Houndsfield units. The circular slice of the phantom is visible in green with concentric circle artifacts. The yellow circles with different intensities indicate the locations of the holes with the contrast medium. The background is in dark blue.

6.3 Contrast Medium in the Reconstructed Image

In the previous chapter, the pixel values of the circles in the reconstructed image that are identified containing different concentrations of contrast medium were calculated. Now, they are plotted over the respective concentration of molybdenum in Figure 6.13. The

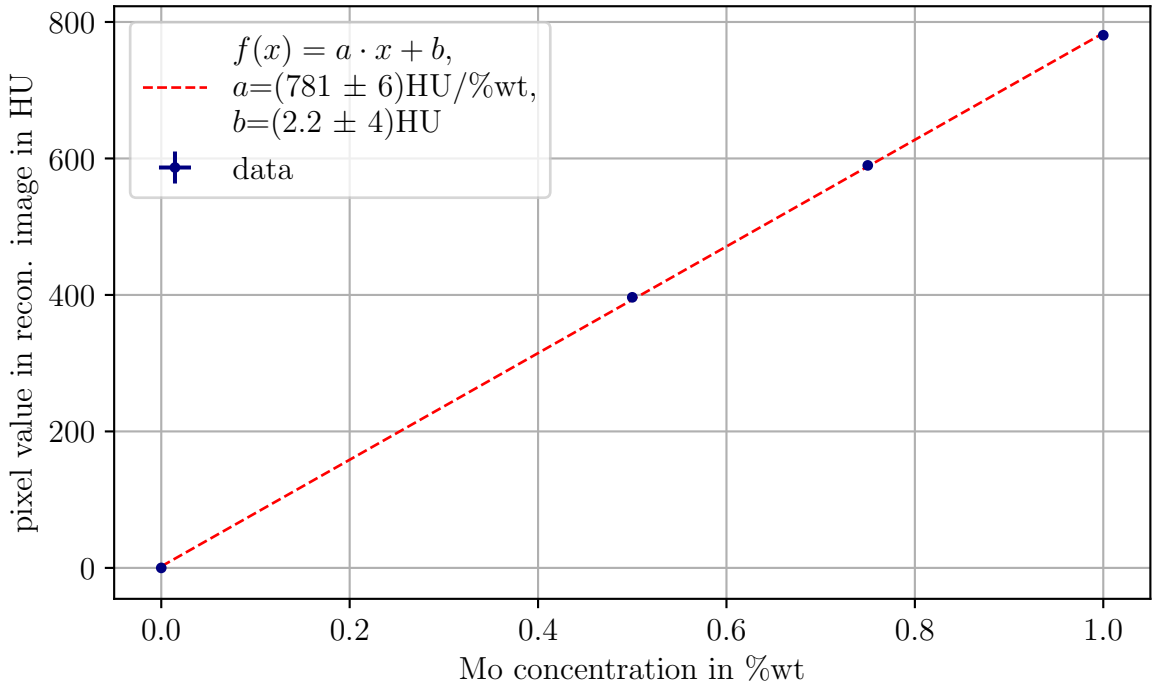

Figure 6.13: Molybdenum concentration of the drilled holes in the phantom over mean pixel values of the respective areas in the backprojected image in Houndsfield units.

errors to the data points are too small to be seen directly in the graphic. As expected, the relation between pixel value and concentration can be approximated by a linear fit through the data points. The fit is shown in the red dashed line. Also, the fit parameters are given in the legend. This finding is in line with the expected linear dependency according to the Lambert-Beer law.

6.4 Conclusion

In this chapter, the first CT scan with Dosepix is performed. The small sensor surface of Dosepix does not allow for capturing the attenuation profile of the utilized phantom in one scan. Hence, it is scanned step wise. The corresponding integral attenuation projections for each projection angle are calculated after the data acquisition and a filtered backprojection is performed to obtain the reconstructed image of the scanned phantom. The reconstructed

image is calibrated to Houndsfield units and the analysis of the reconstructed image shows that the experimental results align with the Lambert-Beer law. Thus, a successful first approach towards applying Dosepix as a detector for medical imaging is presented.

Further examinations are necessary regarding the ringlike artifacts in the reconstructed image. One approach to solve this problem is to investigate the experimental results for continuous scanning of the X-ray transmission profiles along the y-axis of the experimental setup to find whether the current scanning procedure might be its origin.

7 X-Ray Fluorescence Measured with Dosepix

Contents

In this chapter, the X-ray fluorescence (XRF) measurements at three different detector positions for complete rotations of the photon are presented. The utilized detector is the previously introduced Dosepix detector. All measurements are performed utilizing a cylindrical phantom containing contrast medium. The angular dependency of the X-ray fluorescence signal of the phantom rotation angle as well as the detector position is analyzed. Furthermore, the resulting CT image and the experimental results on XRF are brought into context.

7.1 Experimental Results of the Fluorescence Measurement

The following pages contain the experimental results on the X-ray fluorescence measurement of the cylindrical phantom introduced in section 4.3. All results are obtained with the Dosepix detector. The focus hereby lies within the data acquisition, processing, and subsequent analysis.

7.1.1 Experimental Setup and Data Acquisition

The XRF measurements are carried out with a modification of the setup introduced in chapter 6. The XRF configuration requires a different position of Dosepix2. As shown in the schematic illustration depicted in Figure 7.1, Dosepix2 is aligned in radial direction to

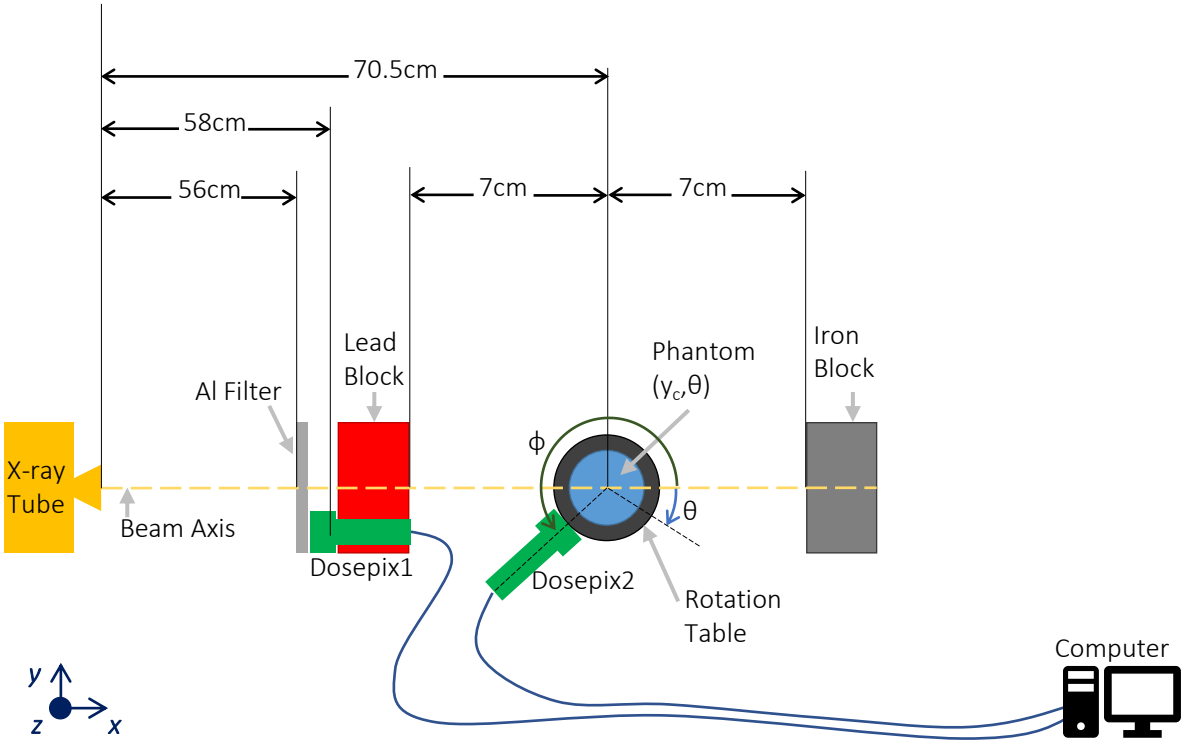

Figure 7.1: Schematic representation of the experimental setup in fluorescence measurement configuration.

the rotation axis of the cylindrical phantom facing perpendicularly towards the center axis of the phantom. The height of Dosepix2 matches the height of the beam axis and there is only minimal distance between phantom and detector cover to allow free rotation of the phantom. This position is characterized by the angle Φ of Dosepix to the beam axis in the xy-plane of the setup. Furthermore, the phantom is located in the center of the beam path y_c along the y-axis during the whole XRF measurement. Only a rotation of the phantom around its vertical center axis is carried out utilizing the rotational table. All other components of the setup presented in chapter 6 remain unchanged. Also, the settings of the LMJ are equal to the X-ray transmission measurements (Table 6.1).

Three fluorescence measurement series are analyzed. Each series differs solely in the angle Φ of the position of the fluorescence detector angle: $\Phi \in [225°, 270°, 315°]$. In each series, the phantom undergoes a full clockwise rotation of 360° around its vertical axis in increments of 1°.

In each rotation position of the phantom, Spec-mode is utilized for the data acquisition with Dosepix2 while a simultaneous Dosi-mode measurement is carried out with the stationary Dosepix1. Spec-mode is a modification of Dosi-mode which enables smaller energy binning over the complete range of the energy deposition spectrum, as described in [9]. The energy binning of Dosepix2 ranges from 10 keV to 70 keV with a bin width of

0.4 keV in the final histogram. The measurement duration of the fluorescence acquisition is chosen in consideration of the work of Johanna Lotter, described in [35]. She utilized a measurement time of 7.5 min to record the fluorescence signal of probes containing 30 ml of molybdenum solution with different mass fractions. Hence, to guarantee sufficiently long measurement times to detect even weak fluorescence signals during a complete rotation of the phantom, 7.5 min is chosen in this thesis as well. This single measurement duration of 7.5 min is divided into 90 frames with a frame time of 5 s. Over the course of one series, the total measurement time accumulates to approximately 47.2 h including the time for rotating the phantom and the waiting time to guarantee synchronized measurements of the two detectors. The sole scan time is 45.0 h per series.

Subsequent to the measurements, all Dosepix2 results are normalized to the corresponding count rate measured with Dosepix1, in order to reduce any adverse effects of fluctuations within the X-ray source.

7.1.2 Extraction of Fluorescence Signal and Relation to CT Scan

A fluorescence measurement with a phantom that consists of PMMA without any additional contrast medium is completed prior to the actual fluorescence phantom. The goal is to get an initial insight on the scattered Compton background of the phantom without additional contrast media. In Figure 7.2, background estimation measurements are shown for all three positions of Dosepix2. All three curves display the same features. The LMJ has a XRF line at 24 keV and the tube voltage is 70 kVp (kilo volt peak). The registered energy deposition spectra correspond to the scattered X-ray spectrum. The reason for the local peaks in the falling slopes is assumed to be artifacts of the spectrum calculation algorithm and require further examination. Hence, in this thesis, they are ignored. Towards lower energies, the falling slopes reach a local minimum at about 15 keV. At energies under 15 keV, the influence of charge sharing increases with decreasing energy, which explains the increase in detected events towards 10 keV. None of the visible peaks corresponds to a molybdenum fluorescence. In case of K_α radiation of molybdenum, a peak at around 17.27 keV [9] (17.38 keV according to the detector calibration shown in chapter 5) is expected. Due to the energy resolution of 1.2 keV of the Dosepix detector [9], the two energies of the $K_{\alpha i}$, $i = 1, 2$, radiation of molybdenum, introduced in section 4.3, will be referred to as one energy denoted with K_α radiation. A measurement example for a fluorescence measurement at Φ=270° and Θ=2° is shown in Figure 7.3. In contrast to the background estimation measurement, the energy deposition spectrum in this figure shows a peak at 16.1 keV, which is identified as the measured molybdenum K_α fluorescence. By means of this figure, the general data processing to extract the fluorescence signal from the energy deposition spectra, is given in the following. Every fluorescence measurement series shown consists of 360 individual measurements which are primarily analyzed for the fluorescence

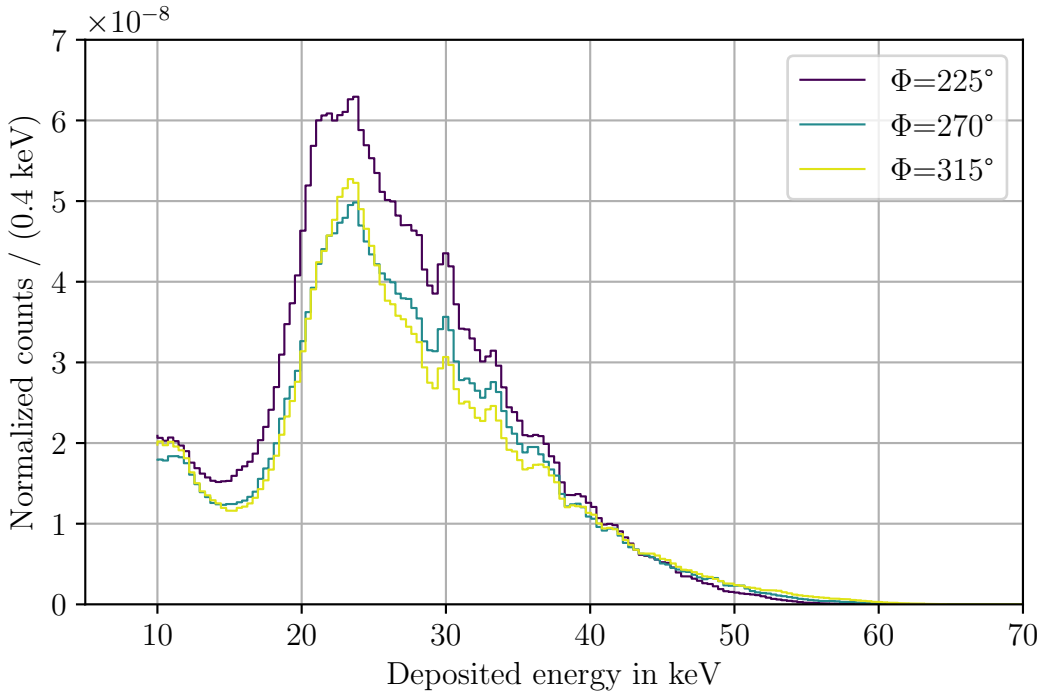

Figure 7.2: Compton background spectrum of a PMMA phantom at the three different detector positions.

peak location automatically. The so found peak position is marked with a dashed gray vertical line. The estimation is used to set an interval of seven bins in each direction and take the linear interpolation (dotted line) of the two endpoints (green). This linear interpolation is further applied as the background cut. A Gaussian fit (dashed red line) is performed on the data in the interval between the two green points after the background cut. The continuous red line marks the mean of the Gaussian fit which coincides with the molybdenum peak of the deposition spectrum. In order to get visual feedback, the Gaussian fit is added to the background cut and plotted in the blue dashed line. The extracted fluorescence signal is the integrated area under the full width half maximum (FWHM) of the Gaussian fit (red dashed line). The FWHM is derived from the Gaussian fit via Equation 7.1, where σ is the standard deviation of the Gaussian fit.

$$\mathrm{FWHM} = 2\sqrt{\ln(2)} \cdot \sigma \tag{7.1}$$

This procedure is applied to all individual measurements in the measurement series with different Dosepix2 positions. The result of the extracted fluorescence signals over the respective phantom rotation angle Θ for all Dosepix2 positions is shown in Figure 7.4. Additionally, the result of the image reconstruction in chapter 6 is given in Figure 7.5.

The error bars are calculated via Gaussian error propagation from the errors of the

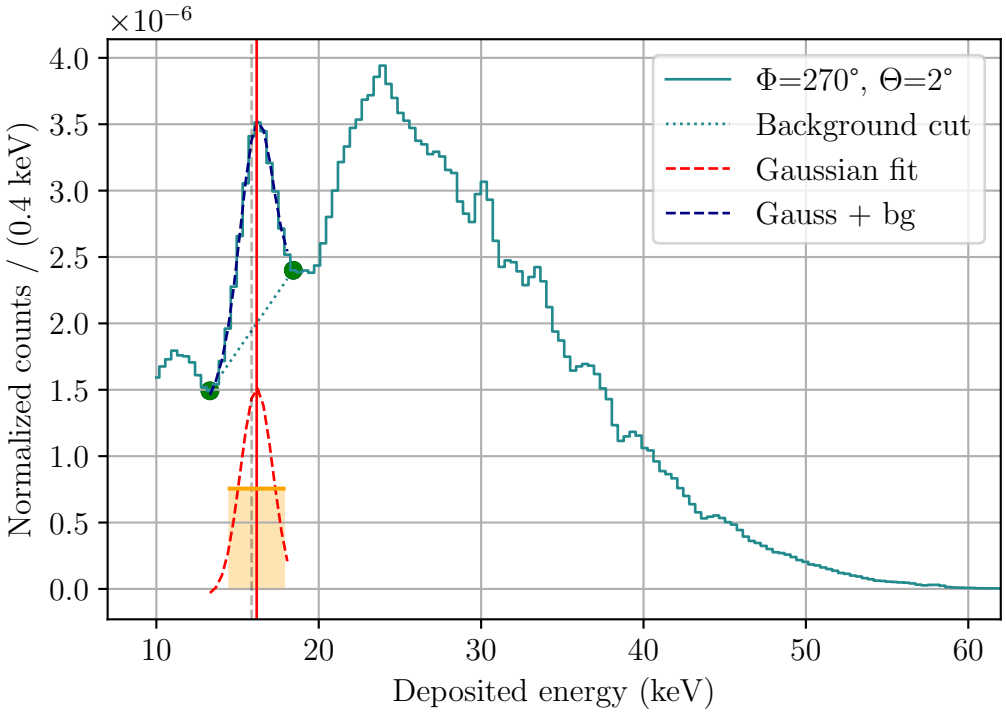

Figure 7.3: Exemplary fluorescence measurement of the Dosepix2 at Φ=270° and the phantom at Θ=2° (in petrol color). The gray dashed line marks the primarily estimated center of the peak caused by fluorescence of the molybdenum. The green points are the neighboring bins which are symmetrically seven bins away from this estimated peak. The dotted line connecting the green points is the linear interpolation between them and is used as an estimate of the background. The fluorescence peak is fitted using a Gaussian peak shape approximation (dashed red line) after subtracting the background from the measured data. The integrated area (FWHM times half peak height of the Gaussian fit) identified with the final fluorescence signal is shown in orange. Blue dashed line is the Gaussian fit plus the background (bg).

respective underlying Gaussian peak formula of each value. The results obtained with the Dosepix2 placed at Φ=225° and Φ=315° show the similar angular dependence with an offset of approximately 180°. The distribution exhibits four different areas of different fluorescence intensity which are equally distributed along Θ. The highest peak in the Φ=225° distribution at approximately Θ=50 indicates that the drilled hole containing a mass fraction of 1.0 wt% is aligned with the beam axis on the most beam sided part of the phantom. Consequently, the drilled hole with 1.0 wt% Mo is located on the adverse side of the phantom, also aligned with the beam axis. This explains the second lowest peak of the Φ=315° measurement series in the vicinity of Θ=50°. In Table 7.1, the corresponding minimum, maximum and the difference between the two values (contrast) are given for each curve. The measurement with the Dosepix2 located at Φ=225° yields the highest

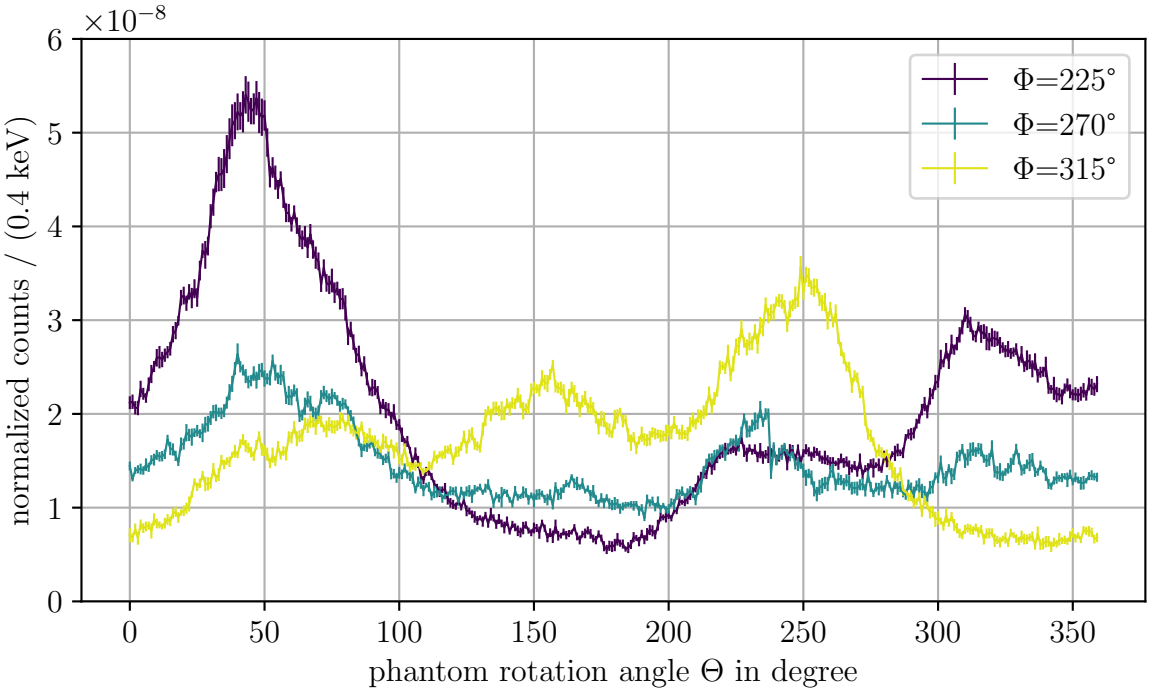

Figure 7.4: Calculated fluorescence signals for the three different Dosepix2 positions. The errors are derived by Gaussian error propagation of the errors to the fit parameters used to calculate the fluorescence signal.

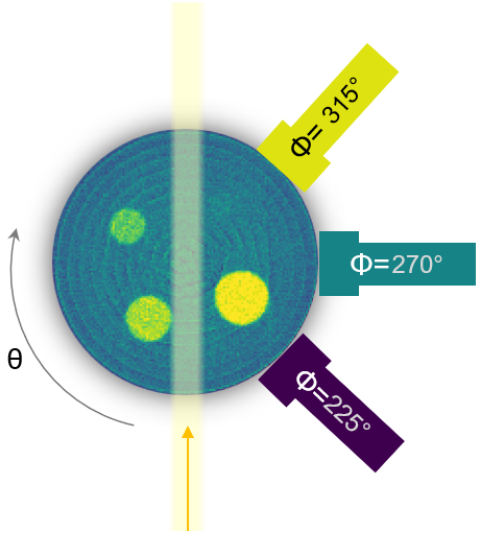

Figure 7.5: The reconstructed image of chapter 6 in the position Θ=0°. The transmission detector positions are shown as well. The yellow arrow marks the beam direction and the transparent yellow rectangle shows the irradiated beam path.

contrast while the one at Φ=270° yields the worst. In the latter case, the Dosepix2 is arranged perpendicularly to the beam axis. Hence, the low contrast is most likely a result of the symmetric ray traces of the fluorescence photons emitted at the irradiated area along beam axis. This means that fluorescence which is created close to the beam at Θ=50° and, on the adverse side of the phantom, at Θ=230°, travels approximately the same distance to the detector arranged perpendicularly to the beam axis at Φ=270°. Hence, the self-absorption inside the phantom is similar and the signal contrast within the measurement series is lowered. Additionally, parts of the phantom closer to the beam are irradiated with higher intensity than parts of the phantom that further away from the beam. This is a consequence of the Lambert-Beer law (Equation 3.2). For this reason, the Dosepix2 at Φ=225° shows the highest contrast, as it is the detector nearest to the X-ray source.

The fluorescence measured at Φ=270° shows an abnormality at Θ=237°. The signal decreases abruptly which is a result of a new initialization of the measurement. The interruption time was approximately 12 h and the abrupt decrease of the signal cannot be explained with the current results. Therefore, in the next section, the time dependency of the fluorescence signal is examined.

Φ	min.	max.	max.-min.
225°	0.55	5.40	4.85
270°	0.89	2.64	1.75
315°	0.58	3.56	2.98

Table 7.1: Minimum and maximum value of normalized counts as well as the difference between both values of normalized counts for the respective measurement series to the corresponding Φ.

7.1.3 Time Dependency of the Fluorescence Signal

Temporal fluorescence signal shift over time was examined using a longtime measurement. Typical causes for a signal shift is thermal shift due to the increased heat load of Dosepix detector during data acquisition.[37][40] The time-stability experiment presented here is carried out by repetition of a measurement at unchanged setup conditions. The overall duration is approximately 24 h with a cool down time of 20 min before initialization. The phantom is located at Θ = 0° and the Dosepix2 at Φ =225°. Positioning of both is kept constant during measurement. In Figure 7.6, the time dependencies of the fluorescence signal, the peak position in the acquired histogram and the calculated FWHM of the Gaussian fit are shown in blue with the corresponding uncertainty interval while the mean value to each quantity is plotted in red with the corresponding 1σ-interval. It is

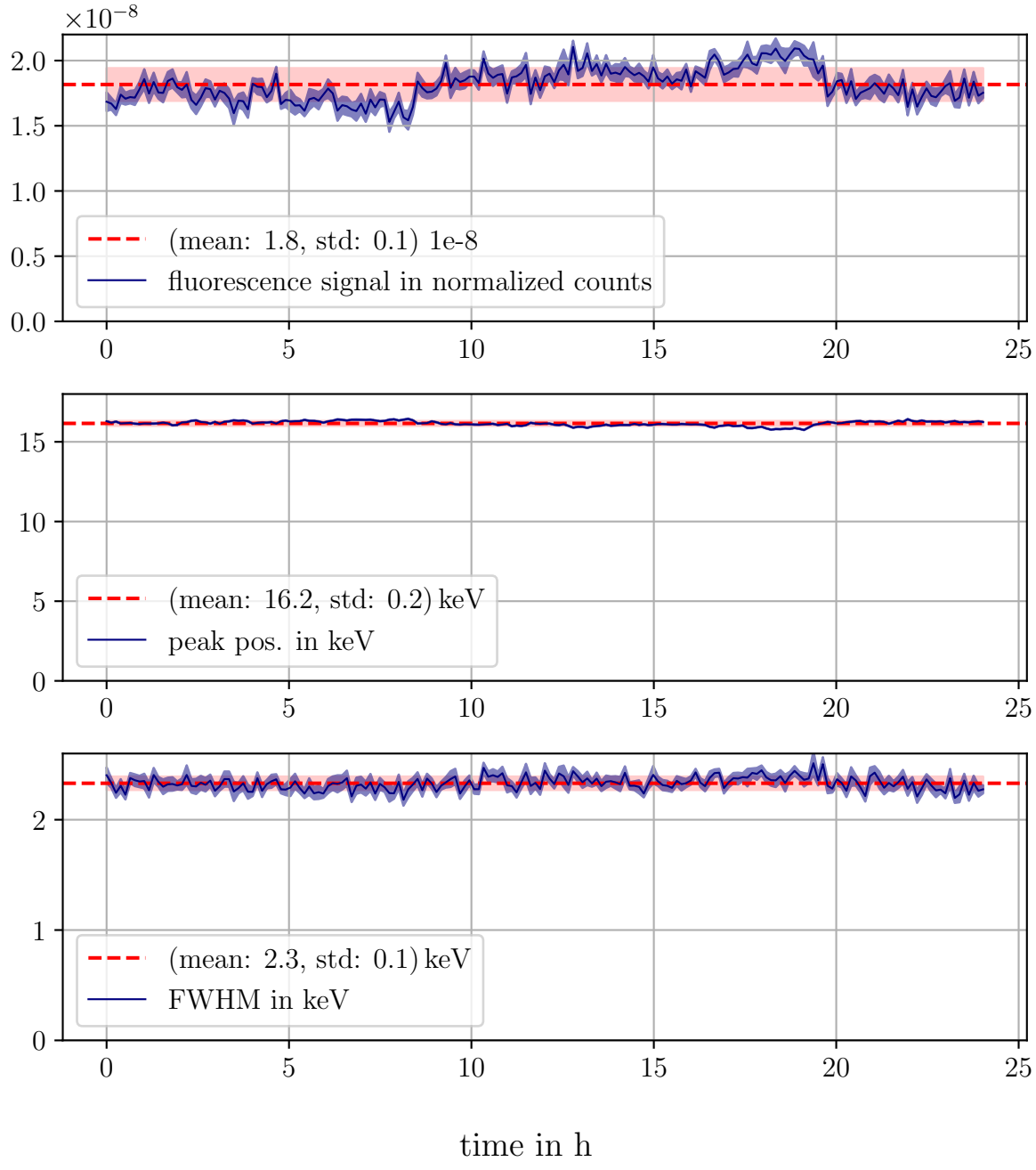

Figure 7.6: Time dependencies of different characteristic quantities from top to bottom: the fluorescence signal (in normalized counts), the peak position (in keV) and the FWHM (in keV). Positioning of the phantom at $\Theta = 0°$ and the Dosepix2 at Φ =225° is kept constant during measurement.

not possible to determine a trend from the measured data. Further examinations should be considered to proof whether the cool down phase of only 20 min is sufficient to get a representative time dependency of the signal.

7.2 Conclusion

In this chapter, dependency of the fluorescence signal on the phantom rotation angle is investigated for different detector positions and discussed in context with the reconstructed image of the previous chapter. Both Dosepix detectors were operated in Dosi-Mode. Dosepix1 utilized identical bin edges for all active large pixels in order to monitor the stability of the flux of the X-ray tube enabling normalization of the XRF detector. Dosepix2 was used for the XRF measurement which required finer binning without loss of count rate information. Therefore, the shifted bin edges method presented in [9] was utilized.

The best results are obtained with the fluorescence detectors placed at 225° and 315° with respect to the beam axis. The contrast within those measurement results is higher than within the measurement results obtained with Dosepix2 at Θ=270°.

The challenges for the measurements are the comparability as well as the reproducibility. There are several factors impeding both challenges, such as the fluctuations of the X-ray source and rising temperature in the readout electronics of the detector during data acquisition. Fluctuations of the X-ray source are inevitable due to the fixed setup. The cooling system of the laboratory is designed to reduce those fluctuations to a minimum. Even if the longtime measurement showed that there is no obvious trend for the time dependency of the fluorescence signal over the duration of a 24 h+ measurement, the temperature stability of Dosepix in the course of long exposure measurements should be further investigated. However, it has to be considered that the cool down phase of 20 min before starting the longtime measurement might not have been enough start a representative measurement.

8 Conclusion and Outlook

In this thesis, a first approach towards XFCT is achieved with Dosepix. A first CT scan is successfully presented: a filtered backprojection method is applied to X-ray transmission scans performed with the Dosepix detector. Furthermore, the angular dependency of molybdenum fluorescence was measured with Dosepix for different angular detector and phantom positions and discussed in the context of the results obtained from the CT scan.

The measurements performed in this thesis provide essential groundwork towards XFCT with Dosepix. However, additional investigations are required to further evaluate the capabilities and limitations of Dosepix for X-ray imaging systems. For example, it is necessary to scan various phantoms of different materials, ideally with soft tissue and bone analogy regarding X-ray attenuation behavior. Also, long measurement durations cause slow improvement cycles. Especially in the transmission measurements, instead of step wise scanning, a continuous scanning approach with constant movement of the phantom along the y-direction for each projection angle has potential to not only lead to faster completion of the scan but might also solve the problem of ringlike artifacts. Furthermore, identifying the minimal scan time for the fluorescence measurements prior to the measurement series potentially leads to a decrease in total measurement duration, as well.

To back-relate the fluorescence signal to location and concentration of the radiation source, further calculations and information on the setup are required, e.g. a beam intensity map of the irradiated area. Larsson et al. state in [12] that a multiplicative SIRT (Simultaneous Iterative Reconstruction Technique) is suitable to reconstruct final fluorescence images from a calculated forward projection matrix and the measured fluorescence signal. The forward projection matrix is derived combining various information on the setup.

In conclusion, the results of this thesis demonstrate that Dosepix presents a promising solution for XFCT, laying the ground for future promising research on this topic.

Literature

[1] W. Schlegel, C.P. Karger, and O. Jäkel. *Medizinische Physik: Grundlagen - Bildgebung - Therapie - Technik*. Springer Berlin Heidelberg, 2018. ISBN: 9783662548011.

[2] T.M. Buzug. *Computed Tomography: From Photon Statistics to Modern Cone-Beam CT*. Springer, 2008. ISBN: 9783540394075.

[3] Jianghong Rao, Anca Dragulescu-Andrasi, and Hequan Yao. "Fluorescence imaging in vivo: recent advances". In: *Current opinion in biotechnology* 18.1 (2007), pp. 17–25.

[4] Michael Schäferling. "The Art of Fluorescence Imaging with Chemical Sensors". In: *Angewandte Chemie International Edition* 51.15 (2012), pp. 3532–3554. DOI: https://doi.org/10.1002/anie.201105459. URL: https://onlinelibrary.wiley.com/doi/abs/10.1002/anie.201105459.

[5] R Ballabriga, M Campbell, and X Llopart. "An introduction to the Medipix family ASICs". In: *Radiation Measurements* 136 (2020), p. 106271.

[6] Roberto Dinapoli et al. "EIGER: Next generation single photon counting detector for X-ray applications". In: *Nuclear Instruments and Methods in Physics Research Section A: Accelerators, Spectrometers, Detectors and Associated Equipment* 650.1 (2011). International Workshop on Semiconductor Pixel Detectors for Particles and Imaging 2010, pp. 79–83. ISSN: 0168-9002. DOI: https://doi.org/10.1016/j.nima.2010.12.005. URL: https://www.sciencedirect.com/science/article/pii/S0168900210027427.

[7] Ch Broennimann et al. "The PILATUS 1M detector". In: *Journal of synchrotron radiation* 13.2 (2006), pp. 120–130.

[8] W. Wong. "A hybrid pixel detector asic with energy binning for real-time, spectroscopic dose measurements". Mid Sweden University, Department of Information Technology and Media, 2012. Ph.D. Thesis.

[9] S. Schmidt. "Dosimetry and X-ray spectroscopy with the photon counting pixel detector Dosepix". Friedrich-Alexander-Universität Erlangen-Nürnberg (FAU), 2021. Ph.D. Thesis.

[10] Magdalena Bazalova et al. “Investigation of X-ray Fluorescence Computed Tomography (XFCT) and K-Edge Imaging”. In: *IEEE Transactions on Medical Imaging* 31.8 (2012), pp. 1620–1627. DOI: 10.1109/TMI.2012.2201165.

[11] Kian Shaker et al. “Longitudinal In-Vivo X-Ray Fluorescence Computed Tomography With Molybdenum Nanoparticles”. In: *IEEE Transactions on Medical Imaging* 39.12 (2020), pp. 3910–3919. DOI: 10.1109/TMI.2020.3007165.

[12] Jakob C Larsson et al. “High-spatial-resolution x-ray fluorescence tomography with spectrally matched nanoparticles”. In: *Physics in Medicine & Biology* 63.16 (Aug. 2018), p. 164001. DOI: 10.1088/1361-6560/aad51e. URL: https://dx.doi.org/10.1088/1361-6560/aad51e.

[13] Amptek. *X-123CdTe Complete X-Ray Gamma Ray Spectrometer*. URL: https://www.amptek.com/internal-products/x-123-cdte-complete-x-ray-gamma-ray-spectrometer-with-cdte-detector.

[14] Amptek. *X-123SDD Complete X-Ray Spectrometer with Silicon Drift Detector (SDD)*. URL: https://www.amptek.com/internal-products/obsolete-products/sdd-x-ray-detectors-for-xrf/x-123sdd-complete-x-ray-spectrometer-with-silicon-drift-detector-sdd.

[15] J. Beutel, H.L. Kundel, and R.L. Van Metter. *Handbook of Medical Imaging*. Handbook of Medical Imaging Vol. 1 Physics and Psychophysics. SPIE - The International Society dor Optical Engineering, 2000. ISBN: 9780819436238.

[16] W. Demtröder. *Experimantalphysik 3 (Atome, Moleküle und Festkörper)*. Springer-Verlag Berlin Heidelberg, 2016. ISBN: 978-3-662-49093-8. DOI: https://doi.org/10.1007/978-3-662-49094-5.

[17] S. Seltzer. *XCOM-photon cross sections database, NIST Standard Reference Database 8*. en. 1987. DOI: 10.18434/T48G6X. URL: http://www.nist.gov/pml/data/xcom/index.cfm.

[18] Lawrence Berkeley National Laboratory. *X-Ray Data Booklet*. 2001. DOI: 10.2172/799621. URL: https://xdb.lbl.gov/.

[19] H. Krieger. *Grundlagen der Strahlungsphysik und des Strahlenschutzes*. Vieweg Teubner Verlag, 2012. ISBN: 978-981-16-5946-1. DOI: 10.1007/978-3-8348-2238-3. URL: https://doi.org/10.1007/978-3-8348-2238-3.

[20] F. E. Zink. “X-ray tubes”. In: *Radiographics* 17 (5 Sept. 1997), pp. 1259–1268. DOI: 10.1148/radiographics.17.5.9308113. URL: https://pubmed.ncbi.nlm.nih.gov/9308113/.

[21] S. Bartzsch and U. Oelfke. "Line focus x-ray tubes—a new concept to produce high brilliance x-rays". In: *Physics in Medicine & Biology* 62.22 (Oct. 2017), p. 8600. DOI: 10.1088/1361-6560/aa910b. URL: https://dx.doi.org/10.1088/1361-6560/aa910b.

[22] Excillum. *Liquid Metall Jet C2*. URL: https://www.excillum.com/our-products/metaljet/.

[23] Oscar Hemberg, Mikael Otendal, and H. Hertz. "Liquid-metal-jet anode electron-impact X-ray source". In: *Applied Physics Letters* 83 (Aug. 2003). DOI: 10.1063/1.1602157.

[24] D. H. Larsson et al. "A 24 keV liquid-metal-jet x-ray source for biomedical applications". In: *Review of Scientific Instruments* 82.12 (2011), p. 123701. DOI: 10.1063/1.3664870. URL: https://doi.org/10.1063/1.3664870.

[25] T. Gabor. "Simulationen und Experimente zur Anwendung eines neuartigen spektroskopischen Pixeldetektors in der Personendosimetrie". Friedrich-Alexander-Universität Erlangen-Nürnberg (FAU), 2012. Diplomarbeit.

[26] D. Haag et al. "Personal Dosimetry in Direct Pulsed Photon Fields With the Dosepix Detector". In: *IEEE Transactions on Nuclear Science* 69 (2022), pp. 2330–2334.

[27] D. Haag. "Active personal dosimetry with the hybrid pixelated DOSEPIX detector". Friedrich-Alexander-Universität Erlangen-Nürnberg (FAU), 2018. Master's Thesis.

[28] F. E. Emery and T. A. Rabson. "Average Energy Expended Per Ionized Electron-Hole Pair in Silicon and Germanium as a Function of Temperature". In: *Phys. Rev.* 140 (6A Dec. 1965), A2089–A2093. DOI: 10.1103/PhysRev.140.A2089. URL: https://link.aps.org/doi/10.1103/PhysRev.140.A2089.

[29] A. Krzyżanowska et al. "Characterization of the Photon Counting CHASE Jr., Chip Built in a 40-nm CMOS Process With a Charge Sharing Correction Algorithm Using a Collimated X-Ray Beam". In: *IEEE Transactions on Nuclear Science* 64.9 (2017), pp. 2561–2568. DOI: 10.1109/TNS.2017.2734821.

[30] Medizinische Physik und Strahlenschutz Budde & Bärenfänger GbR. *Computertomographie (CT)*. URL: https://medizinphysik.wiki/computertomographie/.

[31] ASTRA Toolbox (@astratoolbox7992). *Filtered Backprojection (FBP)*. URL: https://www.youtube.com/watch?v=pZ7JlXagT0w.

[32] National Institute of Standard and Technology. *NIST Chemistry Webbook, SRD 69*. 2023. DOI: https://doi.org/10.18434/T4D303. URL: https://physics.nist.gov/cgi-bin/Star/compos.pl?refer=ap%5C&matno=223.

[33] M.A. Zucker M.J. Berger J.S. Coursey and J. Chang. *NIST Standard Reference Database 124*. DOI: https://dx.doi.org/10.18434/T4NC7P. URL: https://physics.nist.gov/cgi-bin/Star/compos.pl?refer=ap%5C&matno=223.

[34] IAEA - Nuclear Data Section. *Live chart of nuclides*. URL: https://www-nds.iaea.org/relnsd/vcharthtml/VChartHTML.html.

[35] J. Lotter. "Untersuchungen zum Nachweis von Molybdän-Fluoreszenzen mit dem Dosepix-Detektor". Friedrich-Alexander-Universität Erlangen-Nürnberg (FAU), 2021. Bachelor's Thesis.

[36] M. Pushie et al. "Elemental and Chemically Specific X-ray Fluorescence Imaging of Biological Systems". In: *Chemical reviews* 114 (Aug. 2014). DOI: 10.1021/cr4007297.

[37] F. Beißer. "Temperature dependence of the hybrid pixel detector Dosepix with respect to I_{krum} variation". Friedrich-Alexander-Universität Erlangen-Nürnberg (FAU), 2019. Bachelor's Thesis.

[38] *Handbook of Chemistry and Physics Online*. URL: https://hbcp.chemnetbase.com/faces/documents/04_04/04_04_0001.xhtml.

[39] James Anthony Seibert, John M. Boone, and Karen K. Lindfors. "Flat-field correction technique for digital detectors". In: *Medical Imaging 1998: Physics of Medical Imaging*. Ed. by James T. Dobbins III and John M. Boone. Vol. 3336. International Society for Optics and Photonics. SPIE, 1998, pp. 348–354. DOI: 10.1117/12.317034. URL: https://doi.org/10.1117/12.317034.

[40] F. Beißer. "Eye Lens Dosimetry with the Hybrid Photon-Counting Pixel Detector Dosepix". Friedrich-Alexander-Universität Erlangen-Nürnberg (FAU), 2022. Master's Thesis.

Danksagung

Zunächst möchte ich Herrn PD Thilo Michel, Betreuer dieser Arbeit, dafür danken, dass er mir das Thema dieser Masterarbeit angeboten hat und mir ermöglichte diese Arbeit verfassen. Seine Ratschläge und unsere richtungsweisenden Gespräche waren stets hilfreich.

Besonders danken möchte ich Dennis Haag, der mir alle meine Fragen stets geduldig beantwortet hat. Er hat sich besonders in der Endphase der Arbeit die Zeit genommen, mir Sachverhalte auch mehrmals zu erklären. Ebenfalls möchte ich mich bei Florian Beißer und Markus Schneider für die Hilfe bei der praktischen Durchführung der Arbeit, sowie für das gute Arbeitsklima bedanken.

Ein großes Dankeschön gilt meiner Familie und meinem Robi, die mich jederzeit unterstützen. Meinen Freunden möchte ich ebenfalls für die tolle Unterstützung danken.

Selbstständigkeitserklärung

Hiermit erkläre ich, dass ich die vorliegende Arbeit selbstständig angefertigt, nicht anderweitig zu Prüfungszwecken vorgelegt und keine anderen als die angegebenen Hilfsmittel verwendet habe. Sämtliche wissentlich verwendete Textausschnitte, Zitate oder Inhalte anderer Verfasser wurden ausdrücklich als solche gekennzeichnet.

Erlangen, den 06.04.2023

Carolin Kupillas